Characterization of Heterogeneous Coastal Aquifers Using A Deep Learning-Based Data Assimilation Approach

Chenglong Cao[1], Jiangjiang Zhang[1], Wei Gan[2], Tongchao Nan[1], and Chunhui Lu[1]

[1]Hohai University
[2]China University of Petroleum, Beijing

December 27, 2023

Abstract

Seawater intrusion poses a substantial threat to water security in coastal regions, where numerical models play a pivotal role in supporting groundwater management and protection. However, the inherent heterogeneity of coastal aquifers introduces significant uncertainties into model predictions, potentially diminishing their effectiveness in management decisions. Data assimilation (DA) offers a solution by incorporating various types of observational data to characterize these heterogeneous coastal aquifers. Traditional DA techniques, like ensemble smoother using the Kalman formula (ESK) and Markov chain Monte Carlo, face challenges when confronted with the non-linearity, non-Gaussianity, and high-dimensionality issues commonly encountered in aquifer characterization. In this study, we introduce a novel DA approach rooted in deep learning (DL), referred to as ESDL, aimed at effectively characterizing coastal aquifers with varying levels of heterogeneity. We systematically investigate a range of factors that impact the performance of ESDL, including the number and types of observations, the degree of aquifer heterogeneity, the structure and training options of the DL models, etc. Our findings reveal that ESDL excels in characterizing heterogeneous aquifers, particularly when faced with non-Gaussian conditions. Comparison between ESDL and ESK under different experimentation settings underscores the robustness of ESDL. Conversely, in certain scenarios, ESK displays noticeable biases in the characterizing results, especially when measurement data from nonlinear and discontinuous processes are used. To optimize the efficacy of ESDL, meticulous attention must be given to the design of the DL model and the selection of training options, which are crucial to ensure the universal applicability of this DA method.

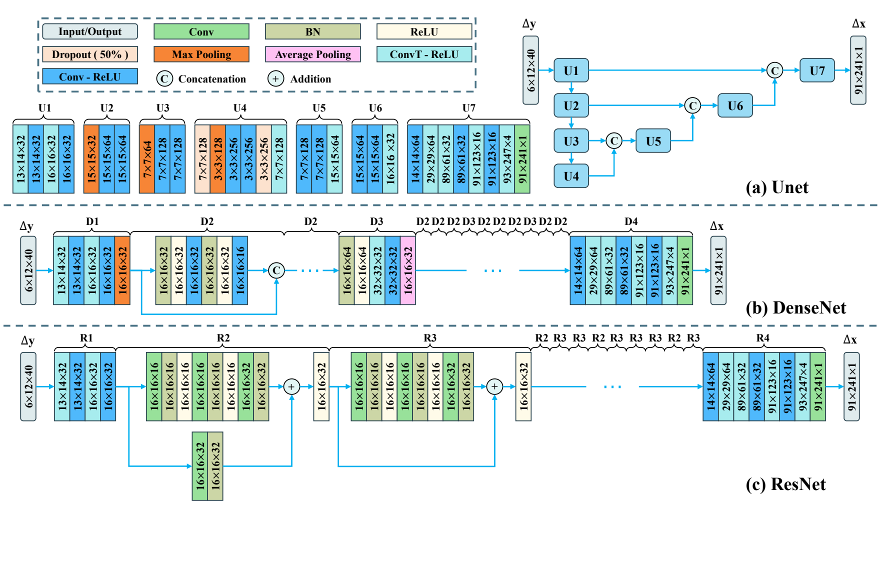

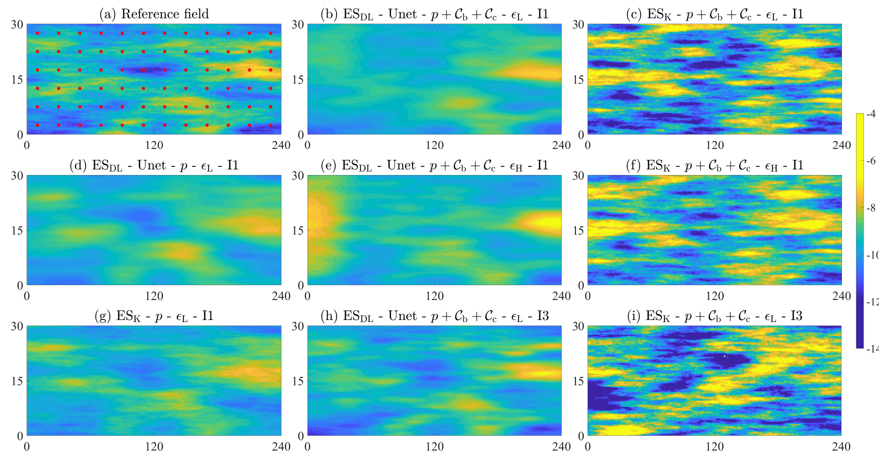
(a) Reference field
(b) $\mathrm{ES_{DL}}$ - Unet - $p + \mathcal{C}_\mathrm{b} + \mathcal{C}_\mathrm{c}$ - ϵ_L - I1
(c) $\mathrm{ES_K}$ - $p + \mathcal{C}_\mathrm{b} + \mathcal{C}_\mathrm{c}$ - ϵ_L - I1
(d) $\mathrm{ES_{DL}}$ - Unet - p - ϵ_L - I1
(e) $\mathrm{ES_{DL}}$ - Unet - $p + \mathcal{C}_\mathrm{b} + \mathcal{C}_\mathrm{c}$ - ϵ_H - I1
(f) $\mathrm{ES_K}$ - $p + \mathcal{C}_\mathrm{b} + \mathcal{C}_\mathrm{c}$ - ϵ_H - I1
(g) $\mathrm{ES_K}$ - p - ϵ_L - I1
(h) $\mathrm{ES_{DL}}$ - Unet - $p + \mathcal{C}_\mathrm{b} + \mathcal{C}_\mathrm{c}$ - ϵ_L - I3
(i) $\mathrm{ES_K}$ - $p + \mathcal{C}_\mathrm{b} + \mathcal{C}_\mathrm{c}$ - ϵ_L - I3
30
15
0
0
120
240
-4
-6
-8
-10
-12
-14

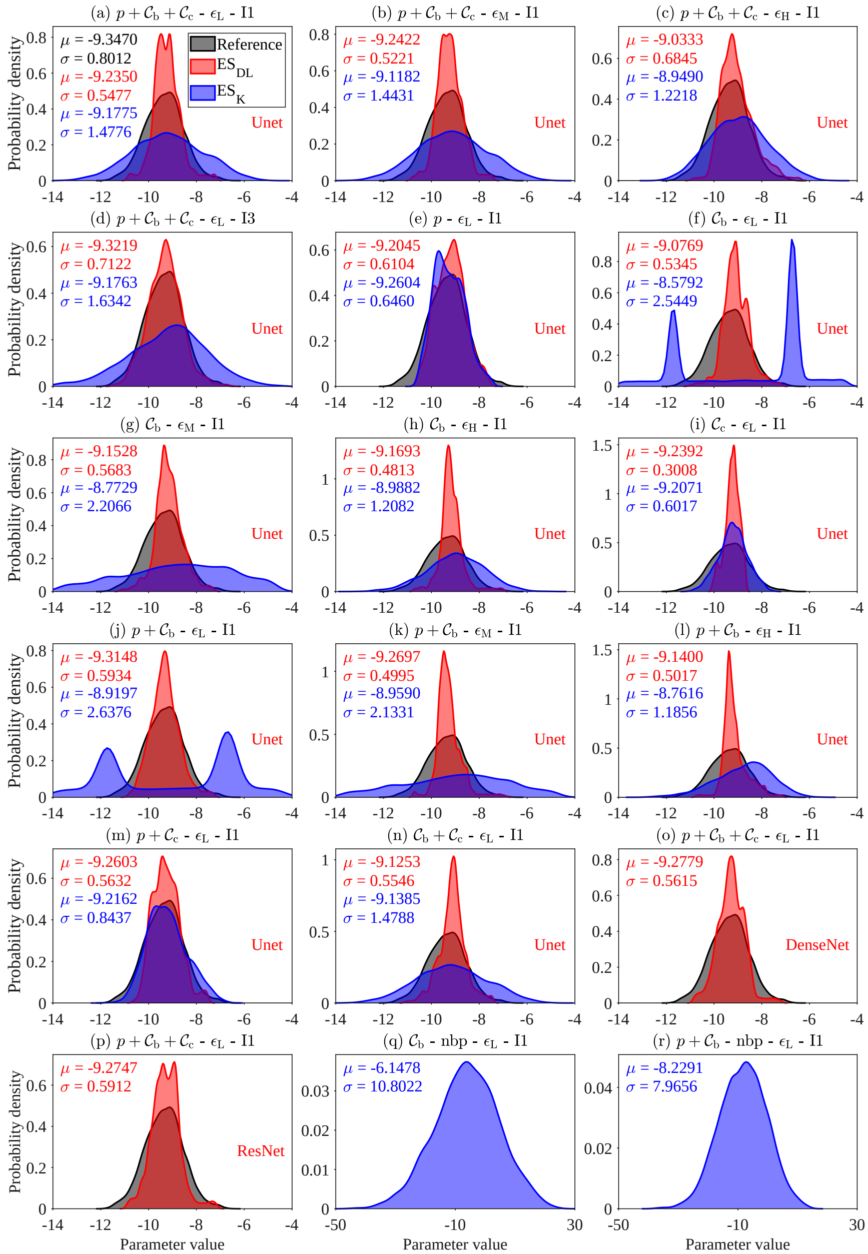
(a) $p+\mathcal{C}_\mathrm{b}+\mathcal{C}_\mathrm{c}$ - ϵ_L - I1
μ = -9.3470
σ = 0.8012
μ = -9.2350
σ = 0.5477
μ = -9.1775
σ = 1.4776
Reference
$\mathrm{ES_{DL}}$
$\mathrm{ES_{K}}$
Unet
(b) $p+\mathcal{C}_\mathrm{b}+\mathcal{C}_\mathrm{c}$ - ϵ_M - I1
μ = -9.2422
σ = 0.5221
μ = -9.1182
σ = 1.4431
Unet
(c) $p+\mathcal{C}_\mathrm{b}+\mathcal{C}_\mathrm{c}$ - ϵ_H - I1
μ = -9.0333
σ = 0.6845
μ = -8.9490
σ = 1.2218
Unet
(d) $p+\mathcal{C}_\mathrm{b}+\mathcal{C}_\mathrm{c}$ - ϵ_L - I3
μ = -9.3219
σ = 0.7122
μ = -9.1763
σ = 1.6342
Unet
(e) p - ϵ_L - I1
μ = -9.2045
σ = 0.6104
μ = -9.2604
σ = 0.6460
Unet
(f) $\mathcal{C}_\mathrm{b}$ - ϵ_L - I1
μ = -9.0769
σ = 0.5345
μ = -8.5792
σ = 2.5449
Unet
(g) $\mathcal{C}_\mathrm{b}$ - ϵ_M - I1
μ = -9.1528
σ = 0.5683
μ = -8.7729
σ = 2.2066
Unet
(h) $\mathcal{C}_\mathrm{b}$ - ϵ_H - I1
μ = -9.1693
σ = 0.4813
μ = -8.9882
σ = 1.2082
Unet
(i) $\mathcal{C}_\mathrm{c}$ - ϵ_L - I1
μ = -9.2392
σ = 0.3008
μ = -9.2071
σ = 0.6017
Unet
(j) $p+\mathcal{C}_\mathrm{b}$ - ϵ_L - I1
μ = -9.3148
σ = 0.5934
μ = -8.9197
σ = 2.6376
Unet
(k) $p+\mathcal{C}_\mathrm{b}$ - ϵ_M - I1
μ = -9.2697
σ = 0.4995
μ = -8.9590
σ = 2.1331
Unet
(l) $p+\mathcal{C}_\mathrm{b}$ - ϵ_H - I1
μ = -9.1400
σ = 0.5017
μ = -8.7616
σ = 1.1856
Unet
(m) $p+\mathcal{C}_\mathrm{c}$ - ϵ_L - I1
μ = -9.2603
σ = 0.5632
μ = -9.2162
σ = 0.8437
Unet
(n) $\mathcal{C}_\mathrm{b}+\mathcal{C}_\mathrm{c}$ - ϵ_L - I1
μ = -9.1253
σ = 0.5546
μ = -9.1385
σ = 1.4788
Unet
(o) $p+\mathcal{C}_\mathrm{b}+\mathcal{C}_\mathrm{c}$ - ϵ_L - I1
μ = -9.2779
σ = 0.5615
DenseNet
(p) $p+\mathcal{C}_\mathrm{b}+\mathcal{C}_\mathrm{c}$ - ϵ_L - I1
μ = -9.2747
σ = 0.5912
ResNet
(q) $\mathcal{C}_\mathrm{b}$ - nbp - ϵ_L - I1
μ = -6.1478
σ = 10.8022
(r) $p+\mathcal{C}_\mathrm{b}$ - nbp - ϵ_L - I1
μ = -8.2291
σ = 7.9656
Probability density
Parameter value

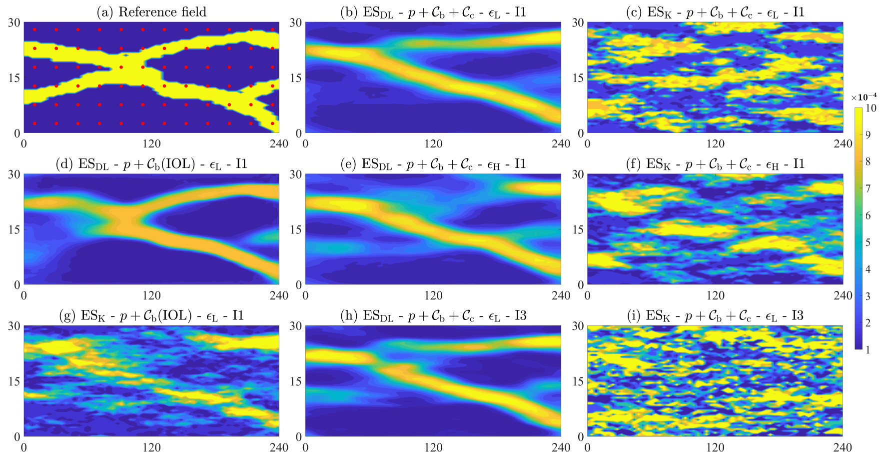

(a) Reference field
(b) $\mathrm{ES_{DL}}$ - $p+\mathcal{C}_\mathrm{b}+\mathcal{C}_\mathrm{c}$ - ϵ_L - I1
(c) $\mathrm{ES_K}$ - $p+\mathcal{C}_\mathrm{b}+\mathcal{C}_\mathrm{c}$ - ϵ_L - I1
(d) $\mathrm{ES_{DL}}$ - $p+\mathcal{C}_\mathrm{b}$(IOL) - ϵ_L - I1
(e) $\mathrm{ES_{DL}}$ - $p+\mathcal{C}_\mathrm{b}+\mathcal{C}_\mathrm{c}$ - ϵ_H - I1
(f) $\mathrm{ES_K}$ - $p+\mathcal{C}_\mathrm{b}+\mathcal{C}_\mathrm{c}$ - ϵ_H - I1
(g) $\mathrm{ES_K}$ - $p+\mathcal{C}_\mathrm{b}$(IOL) - ϵ_L - I1
(h) $\mathrm{ES_{DL}}$ - $p+\mathcal{C}_\mathrm{b}+\mathcal{C}_\mathrm{c}$ - ϵ_L - I3
(i) $\mathrm{ES_K}$ - $p+\mathcal{C}_\mathrm{b}+\mathcal{C}_\mathrm{c}$ - ϵ_L - I3
$\times 10^{-4}$

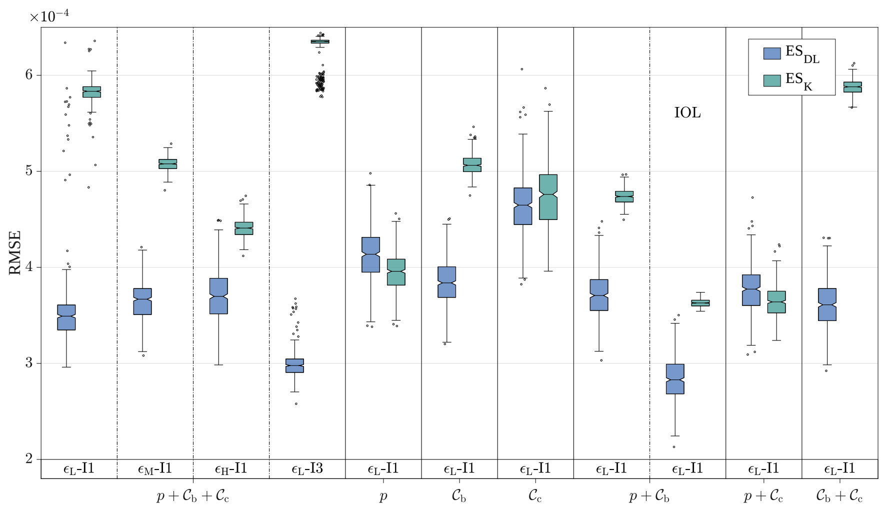

$\times 10^{-4}$
RMSE
$\mathrm{ES_{DL}}$
$\mathrm{ES_K}$
IOL
ϵ_L-I1
ϵ_M-I1
ϵ_H-I1
ϵ_L-I3
$p+\mathcal{C}_\mathrm{b}+\mathcal{C}_\mathrm{c}$
p
$\mathcal{C}_\mathrm{b}$
$\mathcal{C}_\mathrm{c}$
$p+\mathcal{C}_\mathrm{b}$
$p+\mathcal{C}_\mathrm{c}$
$\mathcal{C}_\mathrm{b}+\mathcal{C}_\mathrm{c}$

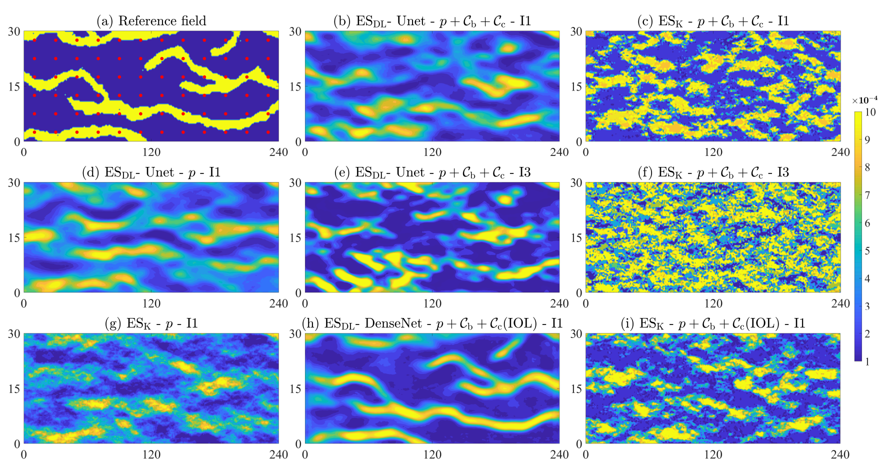

(a) Reference field
(b) $\mathrm{ES_{DL}}$- Unet - $p+\mathcal{C}_\mathrm{b}+\mathcal{C}_\mathrm{c}$ - I1
(c) $\mathrm{ES_K}$ - $p+\mathcal{C}_\mathrm{b}+\mathcal{C}_\mathrm{c}$ - I1
(d) $\mathrm{ES_{DL}}$- Unet - p - I1
(e) $\mathrm{ES_{DL}}$- Unet - $p+\mathcal{C}_\mathrm{b}+\mathcal{C}_\mathrm{c}$ - I3
(f) $\mathrm{ES_K}$ - $p+\mathcal{C}_\mathrm{b}+\mathcal{C}_\mathrm{c}$ - I3
(g) $\mathrm{ES_K}$ - p - I1
(h) $\mathrm{ES_{DL}}$- DenseNet - $p+\mathcal{C}_\mathrm{b}+\mathcal{C}_\mathrm{c}$(IOL) - I1
(i) $\mathrm{ES_K}$ - $p+\mathcal{C}_\mathrm{b}+\mathcal{C}_\mathrm{c}$(IOL) - I1
$\times 10^{-4}$

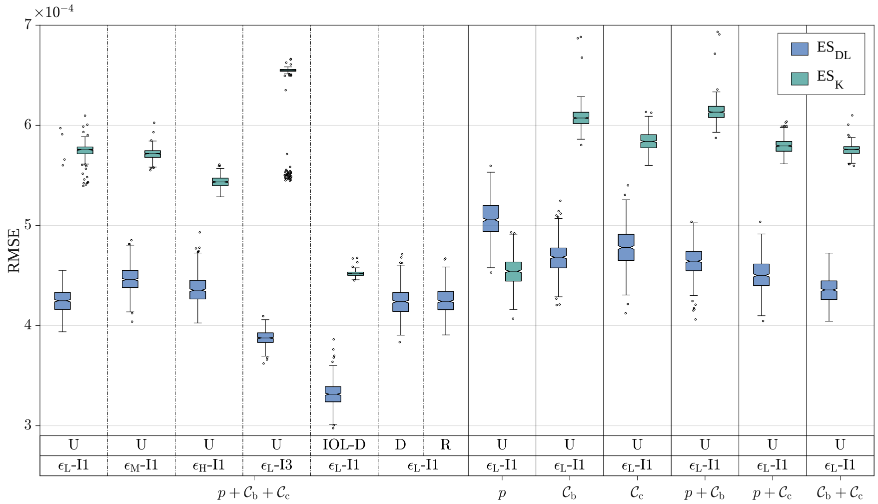

$\times 10^{-4}$
RMSE
$\mathrm{ES_{DL}}$
$\mathrm{ES_{K}}$
U
IOL-D
D
R
ϵ_{L}-I1
ϵ_{M}-I1
ϵ_{H}-I1
ϵ_{L}-I3
$p+\mathcal{C}_{\mathrm{b}}+\mathcal{C}_{\mathrm{c}}$
p
$\mathcal{C}_{\mathrm{b}}$
$\mathcal{C}_{\mathrm{c}}$
$p+\mathcal{C}_{\mathrm{b}}$
$p+\mathcal{C}_{\mathrm{c}}$
$\mathcal{C}_{\mathrm{b}}+\mathcal{C}_{\mathrm{c}}$

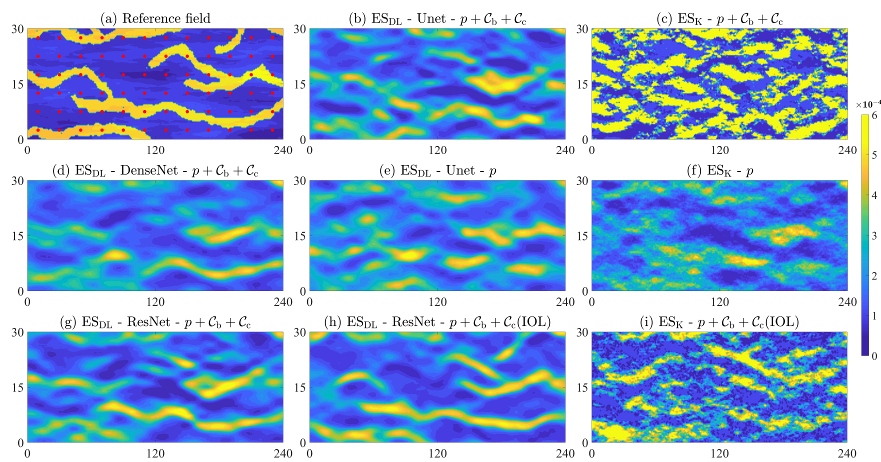

(a) Reference field
(b) $\mathrm{ES_{DL}}$ - Unet - $p+\mathcal{C}_{\mathrm{b}}+\mathcal{C}_{\mathrm{c}}$
(c) $\mathrm{ES_{K}}$ - $p+\mathcal{C}_{\mathrm{b}}+\mathcal{C}_{\mathrm{c}}$
(d) $\mathrm{ES_{DL}}$ - DenseNet - $p+\mathcal{C}_{\mathrm{b}}+\mathcal{C}_{\mathrm{c}}$
(e) $\mathrm{ES_{DL}}$ - Unet - p
(f) $\mathrm{ES_{K}}$ - p
(g) $\mathrm{ES_{DL}}$ - ResNet - $p+\mathcal{C}_{\mathrm{b}}+\mathcal{C}_{\mathrm{c}}$
(h) $\mathrm{ES_{DL}}$ - ResNet - $p+\mathcal{C}_{\mathrm{b}}+\mathcal{C}_{\mathrm{c}}$(IOL)
(i) $\mathrm{ES_{K}}$ - $p+\mathcal{C}_{\mathrm{b}}+\mathcal{C}_{\mathrm{c}}$(IOL)
$\times 10^{-4}$

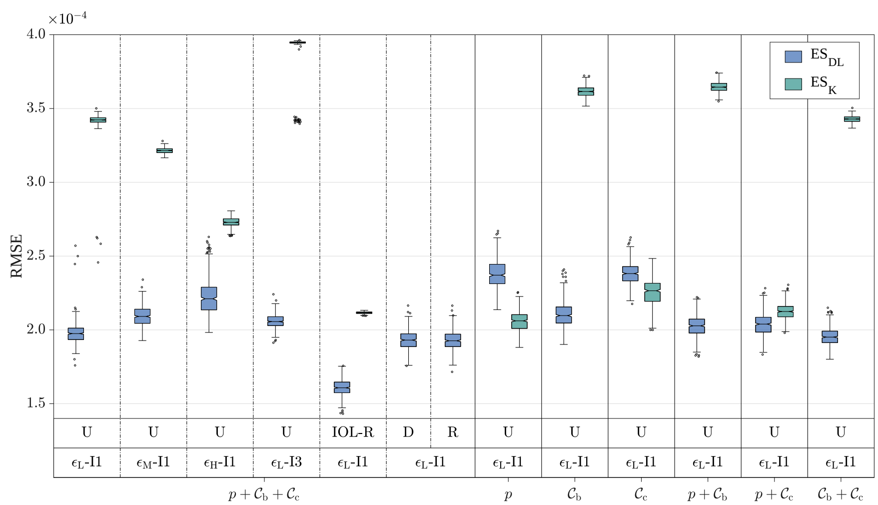

$\times 10^{-4}$
RMSE
$\mathrm{ES_{DL}}$
$\mathrm{ES_{K}}$
U
IOL-R
D
R
ϵ_{L}-I1
ϵ_{M}-I1
ϵ_{H}-I1
ϵ_{L}-I3
$p+\mathcal{C}_{\mathrm{b}}+\mathcal{C}_{\mathrm{c}}$
p
$\mathcal{C}_{\mathrm{b}}$
$\mathcal{C}_{\mathrm{c}}$
$p+\mathcal{C}_{\mathrm{b}}$
$p+\mathcal{C}_{\mathrm{c}}$
$\mathcal{C}_{\mathrm{b}}+\mathcal{C}_{\mathrm{c}}$

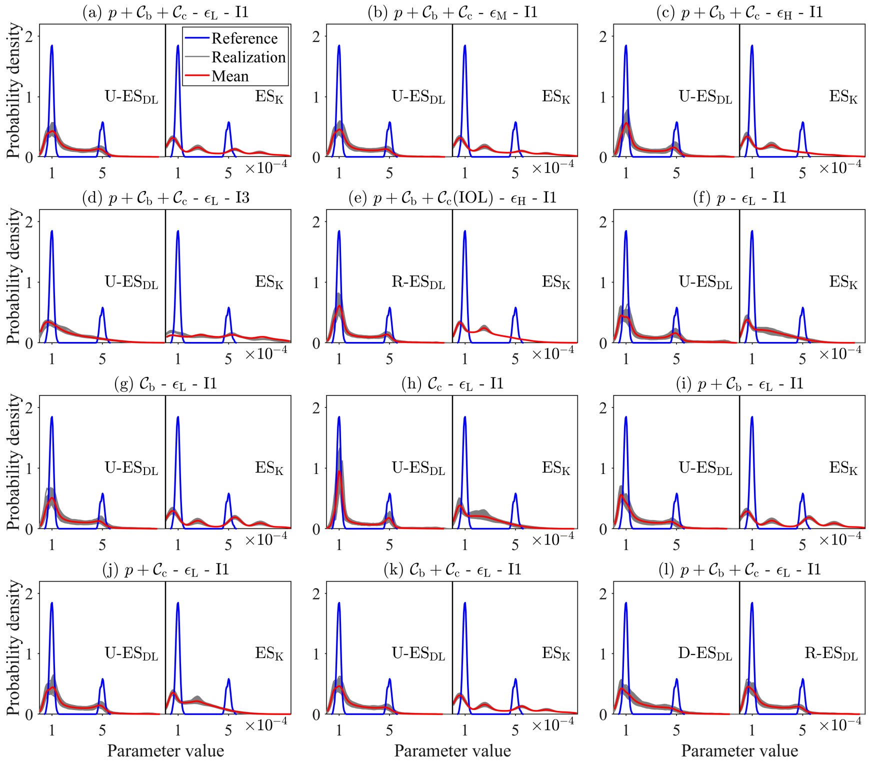
(a) $p + \mathcal{C}_\mathrm{b} + \mathcal{C}_\mathrm{c}$ - ϵ_L - I1
(b) $p + \mathcal{C}_\mathrm{b} + \mathcal{C}_\mathrm{c}$ - ϵ_M - I1
(c) $p + \mathcal{C}_\mathrm{b} + \mathcal{C}_\mathrm{c}$ - ϵ_H - I1
(d) $p + \mathcal{C}_\mathrm{b} + \mathcal{C}_\mathrm{c}$ - ϵ_L - I3
(e) $p + \mathcal{C}_\mathrm{b} + \mathcal{C}_\mathrm{c}$(IOL) - ϵ_H - I1
(f) p - ϵ_L - I1
(g) $\mathcal{C}_\mathrm{b}$ - ϵ_L - I1
(h) $\mathcal{C}_\mathrm{c}$ - ϵ_L - I1
(i) $p + \mathcal{C}_\mathrm{b}$ - ϵ_L - I1
(j) $p + \mathcal{C}_\mathrm{c}$ - ϵ_L - I1
(k) $\mathcal{C}_\mathrm{b} + \mathcal{C}_\mathrm{c}$ - ϵ_L - I1
(l) $p + \mathcal{C}_\mathrm{b} + \mathcal{C}_\mathrm{c}$ - ϵ_L - I1
Reference
Realization
Mean
U-ES_DL
R-ES_DL
D-ES_DL
ES_K
Probability density
Parameter value
$\times 10^{-4}$

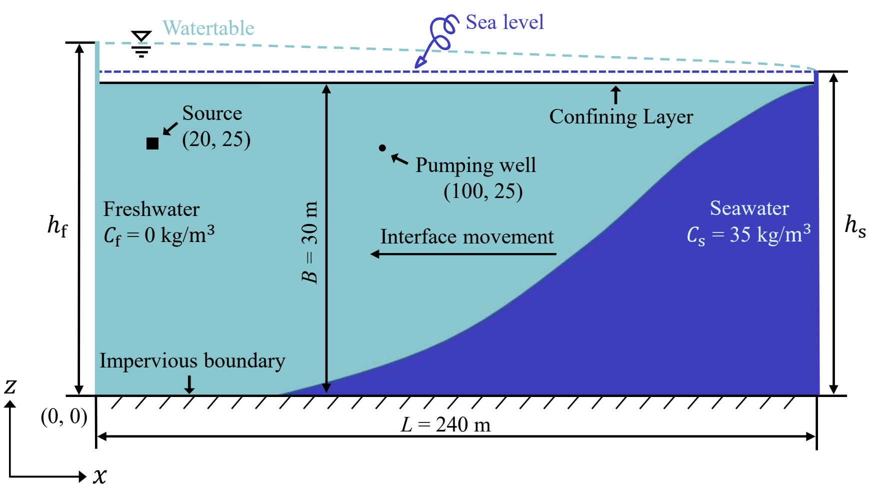
Watertable
Sea level
Source
(20, 25)
Confining Layer
Pumping well
(100, 25)
Freshwater
$C_\mathrm{f} = 0$ kg/m^3
Seawater
$C_\mathrm{s} = 35$ kg/m^3
h_f
h_s
$B = 30$ m
Interface movement
Impervious boundary
z
(0, 0)
$L = 240$ m
x

Characterization of Heterogeneous Coastal Aquifers Using A Deep Learning-Based Data Assimilation Approach

Chenglong Cao[1,2], Jiangjiang Zhang[1,2], Wei Gan[4], Tongchao Nan[1,2], and Chunhui Lu[1,2,3]

[1]Yangtze Institute for Conservation and Development, Hohai University, Nanjing, China,
[2]The National Key Laboratory of Water Disaster Prevention, Hohai University, Nanjing, China,
[3]College of Water Conservancy and Hydropower Engineering, Hohai University, Nanjing, China,
[4]Beijing Key Laboratory of Process Fluid Filtration and Separation, College of Mechanical and Transportation Engineering, China University of Petroleum, Beijing, China

Key Points:

- Non-linearity and non-Gaussianity in coastal aquifer characterization problems pose challenges to traditional data assimilation methods.
- We propose to address these issues with a deep learning-based data assimilation method called $\mathrm{ES_{DL}}$.
- Various factors influencing the performance of $\mathrm{ES_{DL}}$ are systematically investigated.

Corresponding author: Jiangjiang Zhang, `zhangjiangjiang@hhu.edu.cn`

Abstract

Seawater intrusion poses a substantial threat to water security in coastal regions, where numerical models play a pivotal role in supporting groundwater management and protection. However, the inherent heterogeneity of coastal aquifers introduces significant uncertainties into model predictions, potentially diminishing their effectiveness in management decisions. Data assimilation (DA) offers a solution by incorporating various types of observational data to characterize these heterogeneous coastal aquifers. Traditional DA techniques, like ensemble smoother using the Kalman formula (ES_K) and Markov chain Monte Carlo, face challenges when confronted with the non-linearity, non-Gaussianity, and high-dimensionality issues commonly encountered in aquifer characterization. In this study, we introduce a novel DA approach rooted in deep learning (DL), referred to as ES_{DL}, aimed at effectively characterizing coastal aquifers with varying levels of heterogeneity. We systematically investigate a range of factors that impact the performance of ES_{DL}, including the number and types of observations, the degree of aquifer heterogeneity, the structure and training options of the DL models, etc. Our findings reveal that ES_{DL} excels in characterizing heterogeneous aquifers, particularly when faced with non-Gaussian conditions. Comparison between ES_{DL} and ES_K under different experimentation settings underscores the robustness of ES_{DL}. Conversely, in certain scenarios, ES_K displays noticeable biases in the characterizing results, especially when measurement data from nonlinear and discontinuous processes are used. To optimize the efficacy of ES_{DL}, meticulous attention must be given to the design of the DL model and the selection of training options, which are crucial to ensure the universal applicability of this DA method.

1 Introduction

Seawater intrusion (SI) is a critical phenomenon in which seawater infiltrates into freshwater aquifers, leading to the degradation of groundwater quality. SI can arise naturally due to hydraulic connections between seawater and groundwater, but human activities, notably excessive freshwater extraction from coastal aquifers and alterations in land use in coastal regions, can significantly intensify this process (Michael et al., 2005; Riva et al., 2015; Werner et al., 2013; Yu & Michael, 2019). Recent research conducted by Paldor and Michael (2021) indicates that SI may be further exacerbated by factors such as storm surges and climate change, presenting a growing threat to coastal groundwater systems. Alarmingly, about 32% of coastal metropolises, defined as cities located within 150 kilometers of coastlines with populations exceeding one million, are susceptible to SI (T. Cao et al., 2021). The impacts of SI are keenly felt in various regions worldwide, including Europe (Custodio, 2010), Australia (Werner, 2010), China (D. Han & Currell, 2018), and the United States (T. Cao et al., 2021). Effectively managing coastal groundwater resources is imperative to prevent or mitigate the adverse consequences of SI, safeguarding the sustainability of these critical water resources.

In the realm of scientific coastal aquifer management, a variety of modeling techniques have emerged to simulate SI processes across diverse scenarios. These models can be broadly categorized into two primary types: interface models that predominantly rely on analytical solutions, and variable-density models that harness numerical solutions (Coulon et al., 2021; Werner et al., 2013). The pioneering work by Strack (1976) introduced analytical solutions for calculating the maximum safe pumping rate of a single well in a semi-infinite and homogeneous coastal aquifer. Building upon this groundwork, subsequent studies extended these analytical solutions to explore optimal management strategies in scenarios featuring multiple wells. This development laid a scientific foundation for safeguarding coastal aquifers (Lu, Werner, et al., 2013; Mantoglou, 2003; Park et al., 2009; Shi et al., 2020). For complex problems involving nonlinear processes and heterogeneous aquifers, employing numerical models such as SEAWAT (Lu, Chen, et al., 2013), SUTRA (Voss & Provost, 2002), FEFLOW (Michael et al., 2005), and COMSOL Multiphysics (Koohbor et al., 2019) is advisable. These numerical modeling approaches offer a flexible and reliable framework for simulating and forecasting SI processes. Moreover, in recent years, the burgeoning field of deep learning (DL) has garnered substantial attention within SI research (Song et al., 2018; Yang et al., 2023; Yin et al., 2022). This data-driven modeling approach holds immense promise for tackling the intricate challenges in coastal aquifer simulations.

When delving into the study of SI processes, it becomes evident that achieving a robust representation of geological heterogeneity within the simulation models is of paramount importance (Yu & Michael, 2022). Traditionally, since the pioneering work by Freeze (1975), hydraulic conductivity has been assumed to follow a log-normal spatial distribution. However, when dealing with non-Gaussian fields characterized by a diverse array of connectivity patterns, the adoption of multiple-point geostatistics becomes imperative for achieving reasonable subsurface representation (Mariethoz et al., 2010). Coastal aquifers, including channelized and fractured ones, often feature geological structures with intricate connectivity patterns (Folch et al., 2020; Koohbor et al., 2019; Renard & Allard, 2013; Trabucchi et al., 2022; Xu et al., 2022; Yu & Michael, 2019; Zinn & Harvey, 2003). These structures can facilitate preferential flow and exacerbate SI (Geng & Michael, 2020). Consequently, the precise prediction of SI critically hinges on obtaining an accurate estimation of the conductivity field (Zhou et al., 2014). Nonetheless, characterizing these parameters through direct borehole drilling is cost-prohibitive, challenging in capturing the full heterogeneity of the parameter field, and susceptible to the scale-effect issue (Sherlock et al., 2000; Sihag et al., 2019).

To overcome these limitations, researchers can employ indirect observational data, such as hydraulic head (Yoon et al., 2017), solute concentration (Dodangeh et al., 2022), temperature (Blanco-Coronas et al., 2021), and electrical resistivity tomography (ERT; González-Quirós & Comte, 2020), and leverage data assimilation (DA) techniques for effective characterization of heterogeneous aquifers (Goebel et al., 2017; Sendrós et al., 2021). Among the various data types, hydraulic head, particularly the transient measurements, stand out for their ability of capturing fluid flow characteristics and thereby enriching aquifer characterization (P. K. Kang et al., 2017). Complementing this, brine and contaminant concentration data, which encapsulate transport information, indirectly convey crucial flow characteristics and contribute significantly to the understanding of SI processes (P. K. Kang et al., 2017; Yoon et al., 2020). In contrast, temperature and ERT measurements provide a cost-effective and relatively comprehensive observational approach. However, the efficacy of temperature and ERT data is hampered by petrophysical heterogeneity, introducing a notable challenge to their reliability (Blanco-Coronas et al., 2021; González-Quirós & Comte, 2020; Brunetti & Linde, 2018). Moreover, the intricate relationships among these diverse data types add another layer of complexity. Yoon et al. (2020) demonstrated that in SI, fluid flow and solute transport are inherently coupled, fostering shared information between hydraulic head and concentration data. X. Kang et al. (2019) proposed that supplementing abundant yet less reliable ERT data to concentration data can significantly enhance characterization performance. The phenomena of information sharing and complementarity underscore the advantages of assimilating data from multiple sources, as emphasized by relevant research (Beaujean et al., 2014; Folch et al., 2020). Furthermore, the strategic selection of sampling locations plays a pivotal role in maximizing data informativeness. Numerous studies have delved into methodologies such as A-optimality, D-optimality, E-optimality, and relative entropy to optimize observation locations and enhance the overall effectiveness of data collection (Sciortino et al., 2002; Zhang et al., 2015).

Utilizing the available model and measurements, we can leverage DA to fuse the information from the both components, thereby enhancing the prediction accuracy of the model. In the realm of coastal aquifer characterization, the inherent challenges arising from high dimensionality, non-linearity, and non-Gaussian nature pose formidable obstacles, rendering many existing DA methods impractical. For instance, the famous Markov chain Monte Carlo (MCMC) method, while conceptually robust, proves inefficient in solving high-dimensional problems, primarily due to its prohibitive computational cost (Zhang, Vrugt, et al., 2020).

In contrast, the ensemble Kalman filter (EnKF; Evensen, 1994) and its variants like ensemble smoother (ES; Van Leeuwen & Evensen, 1996), which are based on the Gaussian assumption, cannot achieve robust DA results in non-Gaussian conditions (McCurry et al., 2023; Zhang, Zheng, et al., 2020; Zhou et al., 2011). Non-Gaussian challenges in this context can be categorized into two types: those aligning with multi-modal distributions of parameter values, such as the equifinality issue, and those describing parameter fields deviating from Gaussian distributions, exemplified by the conductivity field in a channelized aquifer. To address the former, mitigation options include clustering (Elsheikh et al., 2013) and local updating (Zhang et al., 2018). As for the latter, researchers have proposed to re-parameterize non-Gaussian variables to conform to Gaussian distributions through techniques like normal-score transformation (Li et al., 2018), Gaussian anamorphosis (Schöniger et al., 2012), principal component analysis (Vo & Durlofsky, 2014), discrete cosine transformation (Jung et al., 2017), level set (Chang et al., 2010), or DL (Canchumuni et al., 2017; Z. Han et al., 2022). However, it's crucial to note that the reparameterization and updating process may lead to the loss of certain essential features, and the Gaussian assumption remains inherent in the employed DA methods.

To tackle the prevalent challenge of non-Gaussianity frequently encountered in subsurface characterization problems, we introduced a novel DA method named $\mathrm{ES_{DL}}$ in our earlier work (Zhang, Zheng, et al., 2020). $\mathrm{ES_{DL}}$ harnesses the power of DL to formulate a nonlinear updating scheme to replace the classical Kalman formula, and automatically capture potential non-Gaussian features inherent in the data. Numerical experiments have convincingly demonstrated that $\mathrm{ES_{DL}}$ performs on par with $\mathrm{ES_K}$ (here "K" stands for adopting the Kalman update) in Gaussian scenarios, while exhibiting exceptional proficiency in addressing non-Gaussian challenges. The applicability of the DL-based update in $\mathrm{ES_{DL}}$ has led to its adoption in various applications. For instance, Man et al. (2022) applied $\mathrm{ES_{DL}}$ to estimate heterogeneous soil properties, thereby enhancing risk assessment for vapor intrusion. In another instance, Godoy et al. (2022) replaced the DL model within $\mathrm{ES_{DL}}$ with random forest for estimating subsurface conductivity parameters. A recent study by Zhang et al. (2023) introduced strategies to further enhance the performance of $\mathrm{ES_{DL}}$ in non-Gaussian scenarios. Additionally, Wang and Yan (2022) improved the efficiency of $\mathrm{ES_{DL}}$ in subsurface flow problems by incorporating multi-fidelity simulations. Furthermore, Xiao et al. (2023) adapted $\mathrm{ES_{DL}}$ for predicting future states, instead of parameter estimation, in geological $\mathrm{CO_2}$ sequestration problems. Despite its application across various research domains, several issues remain unaddressed, particularly regarding its application in characterizing heterogeneous coastal aquifers. These include: (1) determining the optimal selection of observational data to enhance $\mathrm{ES_{DL}}$'s performance, (2) identifying the suitable DL model structure and training options, and (3) understanding the impact of varying levels of heterogeneity on the effectiveness of $\mathrm{ES_{DL}}$. Resolving these questions is imperative to offer guidance for the effective implementation of $\mathrm{ES_{DL}}$ in analogous complex problems.

In this paper, we employ the $\mathrm{ES_{DL}}$ method to conduct a comprehensive investigation into the factors influencing its performance in characterizing heterogeneous coastal aquifers with SI. Additionally, the $\mathrm{ES_K}$ method is adopted for comparative analysis. Our study presents a robust experimental framework that encompasses three distinct hydraulic conductivity scenarios: Gaussian fields, binary channelized fields with two distinct conductivity values, and continuous channelized fields conforming to a bimodal Gaussian mixture distribution. Within each scenario, our methodology follows a systematic approach. Firstly, we meticulously compare inversion results using various types of observational data and their combinations. This systematic analysis aims to identify the most informative data types or combinations for our tasks. Secondly, we shift our focus to evaluating the $\mathrm{ES_{DL}}$ method's performance using different widely employed DL network architectures. This phase seeks to pinpoint the network architecture that aligns best with the particular case under consideration. Moreover, the effects of other factor including iteration and measurement error magnitudes are also investigated. The above exploration provides invaluable insights not only in selecting observation data types and network architectures but also in devising ef-

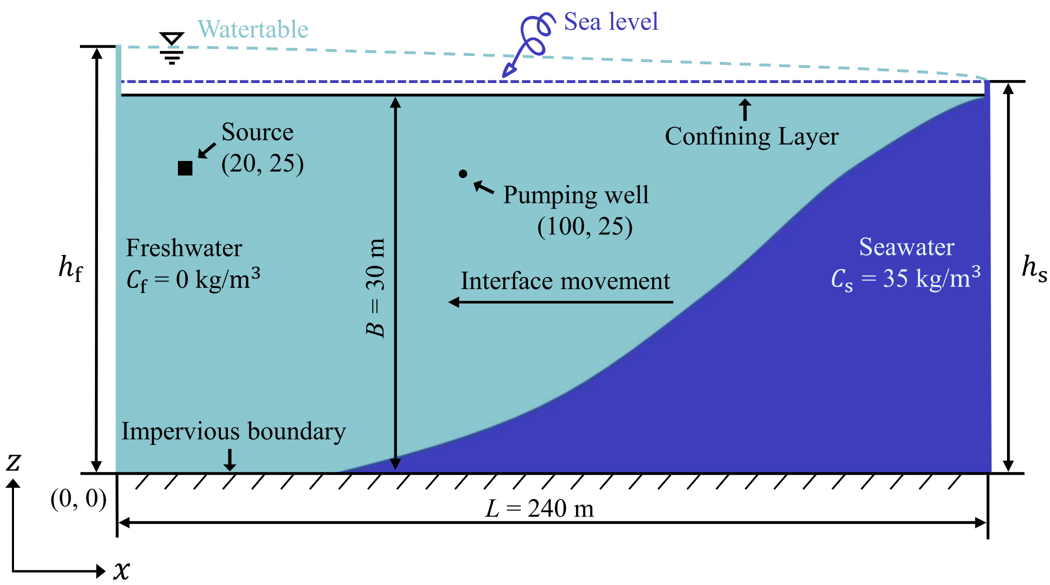

Figure 1. Cross-section of the coastal aquifer with seawater intrusion. The black rectangle signifies a land-based contaminant source, while the black dot represents a pumping well.

fective strategies to address the complexities posed by non-Gaussian fields. In doing so, we aspire to advance the field of coastal aquifer characterization, particularly in the context of SI.

The rest of this paper is structured as follows: In Section 2, we present an overview of the model setup for characterization of coastal aquifer with SI. Section 3 provides the implementation details of both ES_K and ES_{DL} in updating our understanding of the heterogeneous conductivity field using observational data. In Section 4, we undertake a comparative analysis of the inversion results obtained through ES_{DL} and ES_K across varying levels of field heterogeneity. Our focus is on elucidating the factors influencing the algorithm's performance, with particular attention to the unique ability of ES_{DL} in characterizing non-Gaussian fields. Finally, our findings are summarized in Section 5.

2 Model Setups

In this study, we investigate variable-density flow and contaminant transport within a heterogeneous coastal aquifer, as depicted in Figure 1. The domain size measures 240 m$\times$30 m. Initially, the domain is filled with freshwater, maintaining a constant head of 30 m. The upper and lower boundaries of the domain exhibit impermeable conditions. On the left side ($h_f = 31.6$ m$, C_f = 0$ kg/m^3, where the subscript "f" denotes freshwater), and the right side ($h_s = 31.0$ m$, C_s = 35$ kg/m^3, where the subscript "s" denotes saltwater), constant head and (salt) concentration boundaries are specified. This configuration signifies that seawater will gradually migrate from the right to the left. The simulation extends over a period of 4,500 days. A pumping well, with a diameter of 0.5 m and positioned at $\{x = 100$ m$, z = 25$ m$\}$, commences groundwater extraction at a rate of 2 m^3/d after $t = 1,000$ day. During the period from day 1500 to 2500, a land-based conservative contaminant is released at a constant rate of 35 kg/(m$^3\cdot$d) from a square region centered at $\{x = 20.25$ m$, z = 25.25$ m$\}$, with a side length of 0.5 m.

In this study, we employ the following equations to describe the variable-density flow process:

$$\mathbf{u} = -\frac{\mathcal{K}}{\rho g}(\nabla p + \rho g), \tag{1}$$

and

$$\frac{\partial}{\partial t}(\epsilon_{\mathrm{p}}\rho) + \nabla \cdot (\rho \mathbf{u}) = Q_{\mathrm{m}}, \tag{2}$$

where $\mathbf{u}$ (m/s) represents the Darcy's velocity, $\mathcal{K}$ (m/s) denotes the hydraulic conductivity, ∇ means the Nabla operator, p (Pa) is the pore pressure, ρ (kg/m^3) signifies the fluid density, g (m/s^2) is the gravitational acceleration, ϵ_{p} (-) denotes the porosity, and Q_{m} (kg/(m^3·s)) represents the source or sink term, respectively.

The transport of the conservative solute is described by the following equations:

$$\frac{\partial(\epsilon_{\mathrm{p}} C_i)}{\partial t} + \frac{\partial(\rho C_{\mathrm{s},i})}{\partial t} + \nabla \cdot \mathbf{J}_i + \mathbf{u} \cdot \nabla C_i = R_i + S_i, \tag{3}$$

and

$$\mathbf{J}_i = -(D_i + D_{\mathrm{e},i})\nabla c_i. \tag{4}$$

In the above equations, C_i (kg/m^3) represents the concentration of specie i in the liquid, $C_{\mathrm{s},i}$ (-) denotes the proportion adsorbed to solid particles, $\mathbf{J}_i$ (kg/(m$^2 \cdot$ s)) is the mass flux diffusive flux vector, R_i (kg/(m$^3 \cdot$ s)) signifies the reaction rate, S_i (kg/(m$^3 \cdot$ s)) is the source term, $D_{\mathrm{e},i} = \epsilon_{\mathrm{p}}^{4/3} D_{\mathrm{F},i}$ (m^2/s) represents the effective diffusion coefficient, $D_{\mathrm{F},i}$ (m^2/s) denotes the fluid diffusion coefficient, and D_i (m^2/s) denotes the dispersion tensor, respectively. For the study area on the $x-z$ plane, the tensor D_i is made up of the following four components:

$$D_{xx} = \frac{1}{|\mathbf{u}|}\left(\alpha_{\mathrm{L}} u_x^2 + \alpha_{\mathrm{T}} u_z^2\right), \tag{5}$$

$$D_{zz} = \frac{1}{|\mathbf{u}|}\left(\alpha_{\mathrm{L}} u_z^2 + \alpha_{\mathrm{T}} u_x^2\right), \tag{6}$$

$$D_{xz} = D_{zx} = \frac{1}{|\mathbf{u}|}\left(\alpha_{\mathrm{L}} - \alpha_{\mathrm{T}}\right) u_x u_z, \tag{7}$$

where D_{xx}, D_{zz}, D_{xz}, and D_{zx} are the two principal components of the dispersion tensor and their two cross terms, α_{L} and α_{T} specify the longitudinal and transverse dispersivities, u_x and u_z are the water flow velocities in the x and z directions, and $|\mathbf{u}| = \sqrt{u_x^2 + u_z^2}$ is the magnitude of the velocity vector $\mathbf{u}$, respectively. Based on the above settings, we simulate the variable-density flow and contaminant transport processes in heterogeneous coastal aquifers with SI using COMSOL Multiphysics. Here, the uncertainty only stems from the heterogeneous $\mathcal{K}$ field, other parameter values are assumed known from field investigations or laboratory measurements, as listed in Table 1.

3 Methods

For any natural system, we can express the relationship between the observed values of the system, denoted as $\tilde{\mathbf{y}} \in \mathbb{R}^{N_y}$, and the system model, denoted as $\mathcal{F}(\cdot)$, as follows:

$$\tilde{\mathbf{y}} = \mathcal{F}(\mathbf{x}) + \epsilon, \tag{8}$$

where $\mathbf{x} \in \mathbb{R}^{N_x}$ represents the model parameters, $\epsilon \in \mathbb{R}^{N_y}$ denotes the error term. In the coastal aquifer system, the model parameters of interest encompass aquifer properties, the location and release history of contaminant source, and more. Measuring these parameters directly can be challenging. In such cases, DA techniques can be employed to integrate readily available observational data with numerical models, yielding estimates of these unknown parameters. In the following sections, we will introduce two DA methods, namely $\mathrm{ES_K}$ and $\mathrm{ES_{DL}}$, for achieving this purpose.

Table 1. Reference parameter values for porous media and flow/transport processes in the groundwater model with SI.

Parameter	Symbol	Unit	Value
Porosity	ϵ_p	-	0.40
Longitudinal dispersivity	α_L	m	1.00
Transverse dispersivity	α_T	m	0.10
Fluid diffusion coefficient	$D_{\mathrm{F},i}$	m^2/s	1.00×10^{-9}
Seawater density	ρ_s	$\mathrm{kg/m}^3$	1025.00
Freshwater density	ρ_f	$\mathrm{kg/m}^3$	1000.00
Reaction rate	R_i	$\mathrm{kg/(m^3 \cdot s)}$	0.00

3.1 Ensemble Smoother based on the Kalman formula: $\mathrm{ES_K}$

As a variant of the EnKF, $\mathrm{ES_K}$ simultaneously assimilates all observations in a single update, offering practical convenience and computational efficiency for parameter estimation tasks such as subsurface characterization in coastal aquifers. In the implementation of $\mathrm{ES_K}$, N_e sets of parameter samples, denoted as $\mathbf{X}^0 = \{\mathbf{x}_1^0, \ldots, \mathbf{x}_{N_\mathrm{e}}^0\}$, are initially drawn from the prior parameter distribution $p(\mathbf{x})$. Subsequently, each sample $\mathbf{x}_i^0$ $(i = 1, ..., N_\mathrm{e})$ is updated using the Kalman formula as follows:

$$\mathbf{x}_i^1 = \mathbf{x}_i^0 + \mathbf{C}_\mathrm{XY}^0(\mathbf{C}_\mathrm{YY}^0 + \mathbf{R})^{-1}\left(\tilde{\mathbf{y}} + \epsilon_i - \mathcal{F}(\mathbf{x}_i^0)\right), \tag{9}$$

where $\mathbf{X}^1 = \{\mathbf{x}_1^1, \ldots, \mathbf{x}_{N_\mathrm{e}}^1\}$ represents the updated parameter ensemble, $\mathbf{C}_\mathrm{XY}^0$ stands for the cross-covariance between $\mathbf{X}^0$ and $\mathbf{Y}^0 = \{\mathcal{F}(\mathbf{x}_1^0), \ldots, \mathcal{F}(\mathbf{x}_{N_\mathrm{e}}^0)\}$, $\mathbf{C}_\mathrm{YY}^0$ is the auto-covariance matrix of $\mathbf{Y}^0$, and ϵ_i denotes random measurement error conforming to a normal distribution $\mathcal{N}(\mathbf{0}, \mathbf{R})$. The Kalman gain matrix $\mathbf{K}^0 = \mathbf{C}_\mathrm{XY}^0(\mathbf{C}_\mathrm{YY}^0 + \mathbf{R})^{-1}$ defines the Kalman update in $\mathrm{ES_K}$. Notably, this update relies solely on the first two statistical moments, namely the mean and covariance. Furthermore, the mapping defined by $\mathbf{K}^0$ from $\Delta\mathbf{y}_i = \tilde{\mathbf{y}} + \epsilon_i - \mathcal{F}(\mathbf{x}_i^0)$ to $\Delta\mathbf{x}_i = \mathbf{x}_i^1 - \mathbf{x}_i^0$ is linear. Thus, this Kalman-based DA method is constrained by the Gaussian assumption, which can limit its performance in problems involving complex processes and non-Gaussian distributions.

3.2 Ensemble Smoother based on DL: $\mathrm{ES_{DL}}$

To simplify expression, we can express the Kalman update formula as follows:

$$\Delta\mathbf{x}_i = \mathbf{K}^0 \Delta\mathbf{y}_i. \tag{10}$$

If we are able to replace the linear updating scheme defined by the Kalman gain matrix with a nonlinear operator that properly captures potential non-Gaussian characteristics, we can overcome the limitations mentioned above. To achieve this, we introduced a non-linear and non-Gaussian DA method named $\mathrm{ES_{DL}}$ in our previous work (Zhang, Zheng, et al., 2020). In this method, the transformation from $\Delta\mathbf{y}_i$ to $\Delta\mathbf{x}_i$ can be succinctly expressed as follows:

$$\Delta\mathbf{x}_i = \mathcal{G}_\mathrm{DL}^0(\Delta\mathbf{y}_i), \tag{11}$$

where $\mathcal{G}_\mathrm{DL}^0(\cdot)$ denotes the nonlinear relationship acquired through an adequately trained DL model. Utilizing this model, intricate features, such as non-Gaussian properties, embedded within $\Delta\mathbf{x}_i$ and/or $\Delta\mathbf{y}_i$, can be extracted and harnessed for the estimation of model parameters and other relevant quantities.

Training a DL model typically demands a substantial volume of data. In the context of ES_{DL}, we can generate training dataset from $\mathbf{X}^0$ and $\mathbf{Y}^0$ through the following procedure:

$$\Delta\mathbf{X}^0 = \{\mathbf{x}_i^0 - \mathbf{x}_j^0 \,|\, i = 1, \ldots, N_\text{e} - 1,\, i < j \leq N_\text{e}\}, \tag{12}$$

$$\Delta\mathbf{Y}^0 = \{\mathbf{y}_i^0 - \mathbf{y}_j^0 + \epsilon_{ij} \,|\, i = 1, \ldots, N_\text{e} - 1,\, i < j \leq N_\text{e}\}. \tag{13}$$

Here, $\Delta\mathbf{Y}^0$ serves as the input (predictor) to the DL model, $\Delta\mathbf{X}^0$ is the target, and ϵ_{ij} represents a random realization of measurement error. Here, an arbitrary parameter/output set $\{\mathbf{x}_i^0, \mathbf{y}_i^0\}$ in the prior ensemble $\{\mathbf{X}^0, \mathbf{Y}^0\}$ is treated as the true state, based on which we can generate $N_\text{e} - 1$ training data pairs from the rest samples in the prior ensemble. This process enables the creation of a training dataset with $\text{C}_{N_\text{e}}^2 = N_\text{e}(N_\text{e} - 1)/2$ samples, supplying ample data for training the DL model. For instance, with an ensemble size of 500, it becomes possible to generate 124,750 training data pairs.

Once the training of $\mathcal{G}_{\text{DL}}^0(\cdot)$ is completed, we can update each sample in $\mathbf{X}^0$ using the observed data $\widetilde{\mathbf{y}}$ as follows:

$$\mathbf{x}_i^1 = \mathbf{x}_i^0 + \mathcal{G}_{\text{DL}}^0\left(\widetilde{\mathbf{y}} + \epsilon_i - \mathcal{F}(\mathbf{x}_i^0)\right), \tag{14}$$

for $i = 1, ..., N_\text{e}$.

For highly nonlinear problems, it is advisable to perform N_iter iterations for both ES_K and ES_{DL}. The updating schemes at iteration $t = 1, \ldots, N_\text{iter}$ for ES_K and ES_{DL} are as follows:

$$\mathbf{x}_i^t = \mathbf{x}_i^{t-1} + \mathbf{C}_{\text{XY}}^{t-1}\left(\mathbf{C}_{\text{YY}}^{t-1} + \alpha_t\mathbf{R}\right)^{-1}\left(\widetilde{\mathbf{y}} + \sqrt{\alpha_t}\epsilon_i - \mathcal{F}(\mathbf{x}_i^{t-1})\right), \tag{15}$$

$$\mathbf{x}_i^t = \mathbf{x}_i^{t-1} + \mathcal{G}_{\text{DL}}^{t-1}\left(\widetilde{\mathbf{y}} + \sqrt{\alpha_t}\epsilon_i - \mathcal{F}(\mathbf{x}_i^{t-1})\right), \tag{16}$$

where $\alpha_t > 0$ is the inflation factor satisfying $\sum_{t=1}^{N_\text{iter}} 1/\alpha_t = 1$, and $\mathbf{C}_{\text{XY}}^{t-1}$, $\mathbf{C}_{\text{YY}}^{t-1}$, and $\mathcal{G}_{\text{DL}}^{t-1}(\cdot)$ are calculated or trained based on $\mathbf{X}^{t-1} = \{\mathbf{x}_1^{t-1}, \ldots, \mathbf{x}_{N_\text{e}}^{t-1}\}$ and $\mathbf{Y}^{t-1} = \{\mathcal{F}(\mathbf{x}_1^{t-1}), \ldots, \mathcal{F}(\mathbf{x}_{N_\text{e}}^{t-1})\}$. The random errors added to the training data set $\Delta\mathbf{Y}^{t-1}$ are also inflated by a factor of $\sqrt{\alpha_t}$.

To mitigate the occurrence of nonphysical updates, especially in the case of ES_K under specific conditions, we will implement post-processing (or boundary processing) on the updated parameters. Assuming the lower and upper bounds of the parameters are denoted as $\mathbf{x}^\text{low}$ and $\mathbf{x}^\text{up}$, and the prior and updated parameters are represented by $\mathbf{x}^\text{f}$ and $\mathbf{x}^\text{a}$, respectively. In cases where $\mathbf{x}^\text{a} > \mathbf{x}^\text{up}$, we set $\mathbf{x}^\text{a} = (\mathbf{x}^\text{f} + \mathbf{x}^\text{up})/2$. Conversely, if $\mathbf{x}^\text{a} < \mathbf{x}^\text{low}$, we set $\mathbf{x}^\text{a} = (\mathbf{x}^\text{f} + \mathbf{x}^\text{low})/2$. This post-processing step ensures that the updated parameters remain within the reasonable bounds, promoting the physical validity of the results.

3.3 Factors Affecting the Performance of ES_{DL}

Although ES_{DL} has been utilized in various DA applications owing to its superiority over its Kalman counterpart in addressing the non-linear and non-Gaussian challenges, the effectiveness of this DA method can be influenced by several crucial factors. These factors encompass the selection of observational data (such as its type, location, time span, and error level), the degree of subsurface heterogeneity (ranging from Gaussian to non-Gaussian distributions), the specific architecture of the DL model, and the training configurations employed for the DL model, etc. Unfortunately, a comprehensive and systematic evaluation of these factors has been lacking, impeding the method's optimal application in practical scenarios, notably within the context of coastal aquifer characterization, which is indispensable for mitigating issues related to SI. In this study, by conducting an extensive benchmarking analysis, we aim to answer the following questions:

(1) In characterization of coastal aquifers, hydraulic pressure (p), brine concentration (C_b) and contaminant concentration (C_c) have been widely used. However, there remains a lack of clarity regarding the impact of these data on the performance of ES_K and ES_{DL}.

It is conceivable that an improper selection of observational data could adversely affect the outcome of DA. This prompts the following question: What represents the most effective data type or combination thereof for the $\mathrm{ES_{DL}}$ method? Does this choice align with that of $\mathrm{ES_K}$?

(2) In our previous study (Zhang, Zheng, et al., 2020), we have demonstrated that $\mathrm{ES_{DL}}$ outperforms $\mathrm{ES_K}$ when characterizing aquifers with binary channelized parameter fields. However, it remains uncertain whether $\mathrm{ES_{DL}}$ maintains its performance in other non-Gaussian conditions. It is crucial to assess the performance of $\mathrm{ES_{DL}}$, as well as $\mathrm{ES_K}$, in scenarios with varying levels of heterogeneity and non-Gaussianity within the $\mathcal{K}$ field. Identifying the limits of a DA method can offer valuable insights for its practical application. Furthermore, how will iteration affect the performance of $\mathrm{ES_{DL}}$ and $\mathrm{ES_K}$ in this scenario?

(3) As a methodology rooted in DL, the performance of $\mathrm{ES_{DL}}$ depends not only on the complexity of the problem and the choice of observational data but also on the specific DL model constructed for this DA framework. With the continual evolution of DL technology, a diverse range of well-established DL models is available for consideration, such as DenseNet (Huang et al., 2017), ResNet (He et al., 2016), and Unet (Ronneberger et al., 2015). In the context of coastal aquifer characterization challenges, the exploration of DL model architectures and training configurations remains relatively under-explored, especially when tailored to the unique characteristics of the problem and the available data.

4 Case Studies

In this section, we will systematically investigate factors that may affect $\mathrm{ES_{DL}}$'s performance in coastal aquifer characterization, considering varying levels of heterogeneity within the conductivity field. For comparative purpose, we also include results obtained by $\mathrm{ES_K}$. In this section, we establish four cases: the first one involving a Gaussian-distributed parameter field, the second and third ones featuring binary channelized non-Gaussian fields with increasing complexity, and the final one comprising a continuous channelized non-Gaussian field. Within each of these cases, we focus on the influence of various factors on the ability of $\mathrm{ES_{DL}}/\mathrm{ES_K}$ to characterize these heterogeneous parameter fields.

4.1 Case 1: Estimating Gaussian-Distributed Parameter Field

In the first case, we undertake the estimation a Gaussian-distributed parameter field using both $\mathrm{ES_{DL}}$ and $\mathrm{ES_K}$. Under the Gaussian condition, $\mathrm{ES_K}$ is expected to yield reliable results. However, this expectation may not hold true in the context of complex and highly non-linear SI problems. As demonstrated later, the inclusion of the C_b measurements can lead to a significant deterioration in the results obtained by $\mathrm{ES_K}$. Subsequent investigations reveal that the magnitude of measurement error associated with C_b plays a role in influencing the performance of $\mathrm{ES_K}$. In contrast, $\mathrm{ES_{DL}}$ is able to obtain reliable results under various conditions.

In this work, the $\mathcal{K}$ field consistently demonstrates characteristics of both heterogeneity and isotropy across all case studies. In the present case, to adhere to Gaussianity, the target of DA is the $\ln(\mathcal{K})$ field to the base e, as opposed to the $\mathcal{K}$ field itself, with reference values depicted in Figure 2(a). The objective is to estimate the $\ln(\mathcal{K})$ field with diverse measurement data types collected at 6×12 locations denoted by the red dots in Figure 2(a). This comprehensive observational dataset comprises $6\times12\times40$ points, encompassing both p and C_b measurements at 15 moments of $t = 300, 600, ..., 4500$ days, and C_c measurements at 10 moments of $t = 1800, 2100, ..., 4500$ days, respectively.

This case study revolves around four pivotal aspects: (1) the influence of measurement types and their combinations on the performance of both $\mathrm{ES_{DL}}$ and $\mathrm{ES_K}$, (2) the impact of measurement error magnitude on the efficacy of the two DA methods, (3) the potential

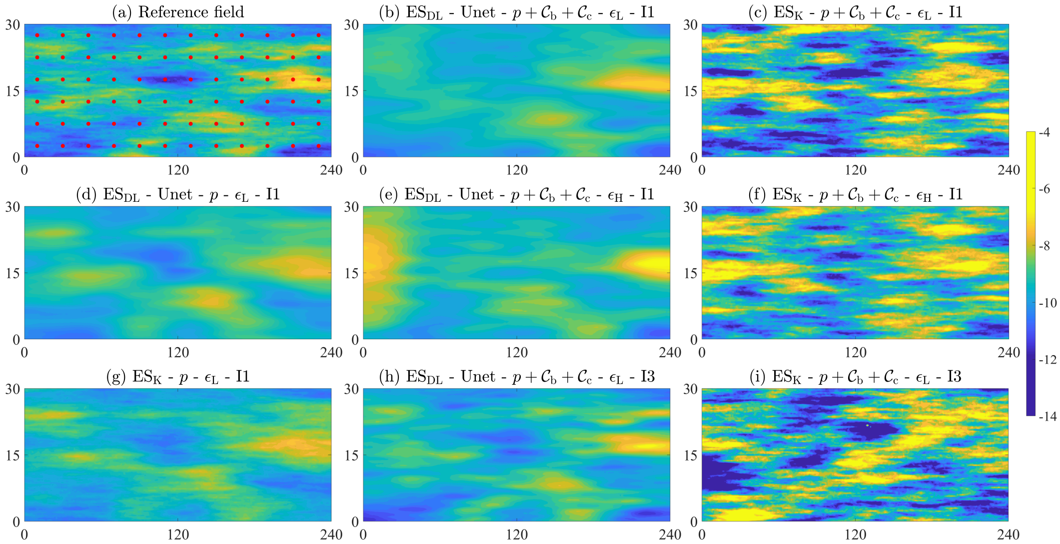

Figure 2. (a) The reference $\ln(\mathcal{K})$ field and the 6×12 locations of observational wells (red dots) in Case 1; (b-i) The mean fields obtained by ES$_{\mathrm{K}}$/ES$_{\mathrm{DL}}$ with different measurement types, error levels (ϵ_{L} for low level and ϵ_{H} for high level), and iteration numbers (I1 for one iteration and I3 for three iterations).

enhancement of algorithm effectiveness through iterations, and (4) the influence of DL model structures and training hyper-parameters on the performance of ES$_{\mathrm{DL}}$. In addressing the first aspect, this investigation incorporates seven types or combinations of observational data for parameter estimation, i.e., "p", "C_{b}", "C_{c}", "p+C_{b}", "p+C_{c}", "C_{b}+C_{c}", and "p+C_{b}+C_{c}", respectively. Concerning the second aspect, the analysis explores the impact of measurement errors by testing three magnitudes: $\epsilon_{\mathrm{L}} \sim \mathcal{N}(0, 0.05^2)$ as the low level, $\epsilon_{\mathrm{M}} \sim \mathcal{N}(0, 0.5^2)$ as the medium level, and $\epsilon_{\mathrm{H}} \sim \mathcal{N}(0, 2^2)$ as the high level (for convenience, all data types use the same distribution for the measurement error). With regard to the third aspect, three iterations are conducted for the "p+C_{b}+C_{c}" observational scenario under the low measurement error condition (note, the other tests perform only one iteration). Finally, the fourth aspect considers the influence of three DL models, namely Unet, DenseNet, and ResNet, along with various training hyper-parameters (as indicated in Table 2) on the performance of ES$_{\mathrm{DL}}$.

Using the "ES$_{\mathrm{DL}}$ - Unet - p+C_{b}+C_{c} - ϵ_{L} - I1" scenario as an example, we provide a concise overview of the method's implementation details. Initially, we generate $N_{\mathrm{e}} = 500$ sets of random parameter samples, denoted as $\mathbf{X}^0 = \{\mathbf{x}_1^0, ..., \mathbf{x}_{N_{\mathrm{e}}}^0\}$, from the prior parameter distribution. Here, $\mathbf{x} \equiv \ln(\mathcal{K})$, and we utilize the sequential Gaussian simulation from GSLIB (Deutsch & Journel, 1998) to generate random realizations of the $\ln(\mathcal{K})$ field, maintaining a mean of $\ln(10^{-4})$ and standard deviation of one. Subsequently, we compute the corresponding model outputs, i.e., $\mathbf{Y}^0 = \{\mathbf{y}_1^0 = \mathcal{F}(\mathbf{x}_1^0), ..., \mathbf{y}_{N\mathrm{e}}^0 = \mathcal{F}(\mathbf{x}_{N\mathrm{e}}^0)\}$. In this context, the parameter has dimensions of 91×241×1, while the model output $\mathbf{y} = \{p, C_{\mathrm{b}}, C_{\mathrm{c}}\}$ has dimensions of 6×12×40. The Unet model is employed to establish the relationship between $\Delta\mathbf{y}$ and $\Delta\mathbf{x}$. The architecture of the Unet model, illustrated in Figure 3(a), includes 2-D convolution (Conv) layers, transposed 2-D convolution (ConvT) layers, max-pooling layers, rectified linear unit activation (ReLU) layers, and other components. With $\mathbf{X}^0$ and $\mathbf{Y}^0$, we can generate training dataset of $\{\Delta\mathbf{y}, \Delta\mathbf{x}\}$ with $N_{\mathrm{e}}(N_{\mathrm{e}} - 1)/2$ samples, which can facilitate the effective training of the Unet model under the training configuration denoted as C1 in Table 2. By inputting the difference between the observed values (perturbed with random measurement error, i.e., $\tilde{\mathbf{y}} + \epsilon$) and the model output (i.e., $\mathbf{y}^0$) into the trained

Table 2. Options (i.e., hyper-parameters, HPs) for training the DL model employed in different tests of this study. Note, HP_1 to HP_5 represent the number of epochs, learning rate, size of mini-batch, gradient threshold, and factor for L_2 regularization, respectively. Here, the ADAM optimizer is used in each test. For different tests, these configurations have been systematically examined so that the ES_{DL} method can obtain reliable results.

Configuration	HP_1	HP_2	HP_3	HP_4	HP_5
C1	50	10^{-3}	128	$+\infty$	1×10^{-4}
C2	50	10^{-3}	512	$+\infty$	1×10^{-4}
C3	100	10^{-3}	128	$+\infty$	1×10^{-4}
C4	100	10^{-3}	64	10	2×10^{-4}
C5	150	10^{-3}	1024	10	2×10^{-4}
C6	100	10^{-3}	512	10	2×10^{-4}
C7	100	10^{-3}	128	10	2×10^{-4}
C8	50	10^{-3}	128	10	2×10^{-4}
C9	50	10^{-3}	256	10	2×10^{-4}

DL model, we can obtain the updated $\ln(\mathcal{K})$ by adding the predicted parameter difference with the prior parameter vector (i.e., $\Delta\mathbf{x}^{\text{pred}} + \mathbf{x}^0$). In alternative scenarios with ES_{DL}, DenseNet and ResNet models depicted in Figures 3(b-c) will be employed, whose training configurations are respectively illustrated in Table 2 as C4 and C5.

Figures 2(b-i) illustrate the mean estimates of $\ln(\mathcal{K})$ obtained through ES_K/ES_{DL} under various settings. Employing the Unet-based ES_{DL} method for assimilating all three types of data (with the error level of ϵ_L) in a single iteration yields a robust estimate of the parameter field (Figure 2b), characterized by an average root mean square error (RMSE) of 0.72 between the obtained posterior ensemble and the reference $\ln(\mathcal{K})$ fields. It is noted here that the average RMSE between the prior $\mathbf{X}^0$ and the reference $\ln(\mathcal{K})$ is 1.16. The reference parameter field's high and low regions are identifiable, although the estimated field appears smoother, lacking characterization of certain fine details. However, utilizing the ES_K method under the same conditions results in a significantly biased estimation, as depicted in Figure 2(c). In this scenario, ES_K tends to overestimate high parameter values and underestimate low parameter values, with a related RMSE of 1.48—considerably higher than that of ES_{DL}, and even the prior ensemble. Increasing the level of measurement error (ϵ_H) marginally improves ES_K's performance, achieving an RMSE of 1.28. Nonetheless, the $\ln(\mathcal{K})$ field remains inaccurately estimated (Figure 2f). In this context, ES_{DL} slightly overestimates parameter values at the left boundary (Figure 2e) but not to a significant extent. After three iterations (with ϵ_L), ES_{DL} demonstrates improved results (RMSE: 0.55), while ES_K continues to produce divergent results (RMSE: 1.78), as depicted in Figures 2(h-i). However, if only the p data are utilized in ES_K, reasonable results can be obtained (Figure 2g), with an average RMSE of 0.77. These findings indicate that ES_K struggles to adequately handle the complex solute transport process in coastal aquifers with SI, characterized by highly non-linear and discontinuous behaviors. This classical method appears effective primarily in situations involving more linear and continuous hydraulic processes (e.g., when only using the p data).

For ES_{DL} with a single iteration, employing "p+C_c+C_b" at different error magnitudes of ϵ_L, ϵ_M, and ϵ_H, the resulting average RMSEs are 0.72, 0.77, and 0.99, respectively, aligning with the typical expectations. When ES_{DL} is implemented with different DL models (p+C_p+C_c - ϵ_L - I1), remarkably similar results are achievable, with RMSEs of 0.72, 0.72, and 0.75 for Unet, DenseNet, and ResNet, respectively. This indicates that a well-designed

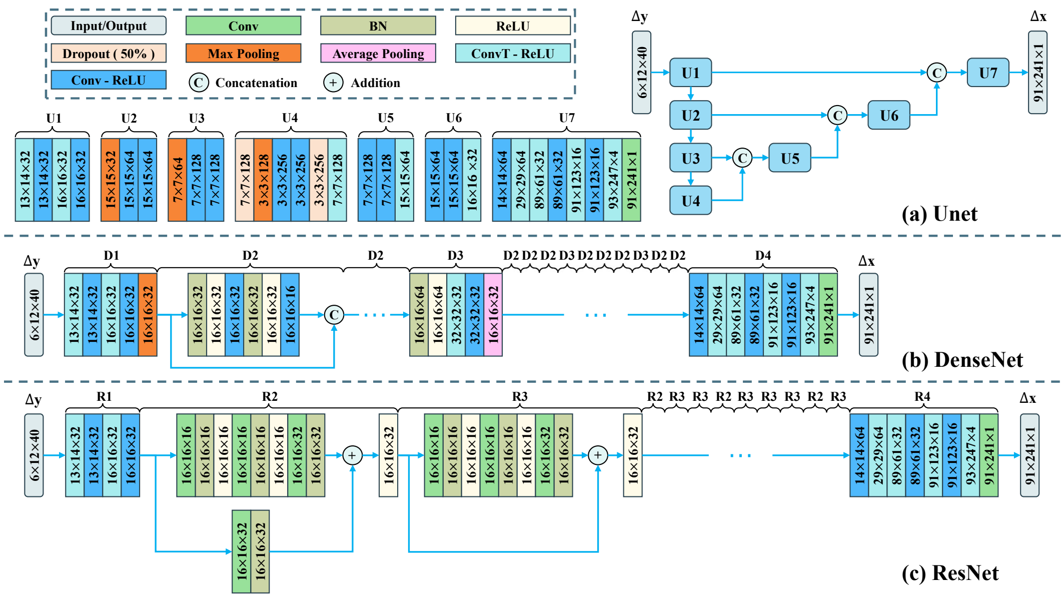

Figure 3. The network structures of (a) Unet, (b) DenseNet, and (c) ResNet, respectively. In each layer, the numbers represent the output sizes in the form of height×width×channels. Conv, ConvT, BN, and ReLU correspond to 2-D convolution layer, transposed 2-D convolution layer, batch normalization layer, and rectified linear unit, respectively. It is worth noting that while the input/output dimensions may vary for different case studies, the network structure remains consistent.

DL model with appropriate training options can yield comparable outcomes. When only a single data type of $p, C_c,$ or C_b is utilized at the low measurement level (ϵ_L), ES_{DL} attains RMSEs of 0.77, 0.86, and 0.93, respectively, suggesting that the p data contain more information about the hydraulic conductivity parameters.

To enable a thorough comparison of the characterization performance between the two algorithms across diverse scenarios, we conduct an analysis of the probability density distributions derived from the estimated mean fields of $\ln(\mathcal{K})$, as depicted in Figure 4. In this representation, the reference field is denoted by the black curve, while the mean fields obtained by ES_{DL} and ES_K are represented by the red and blue curves, respectively. The sub-figure titles are meticulously structured to provide implementation details. Particularly noteworthy is the"nbp" designation, indicating the absence of parameter boundary processing for the updated parameters obtained by ES_K. Moreover, the mean (μ) and standard deviation (σ) of each field are provided in the sub-figures. Upon careful examination of these distribution curves, a significant observation arises: the standard deviation of the mean field obtained through ES_{DL} is markedly smaller than that of the mean field estimated by ES_K. In the comparison of Figures 4(a) and (d), it becomes evident that iterations lead to a better alignment of the probability density curves obtained by ES_{DL} with the reference field. Figures 4(a), (o), and (p) display the distribution of mean fields obtained by ES_{DL} based on three different DL models. The probability density distribution curves reveal that all three DL models perform equally well in inverting the reference field. For ES_K using the "C_b" and "p+C_b" datasets, unexpected bi-modal distributions of $\ln(\mathcal{K})$ are observed in Figures 4(f) and (j). This is caused by the boundary processing of the updated parameters obtained by ES_K. If this boundary processing approach is absent, as shown in Figures 4(q-r), significantly biased results will be obtained, indicating divergence in the Kalman updating outcomes.

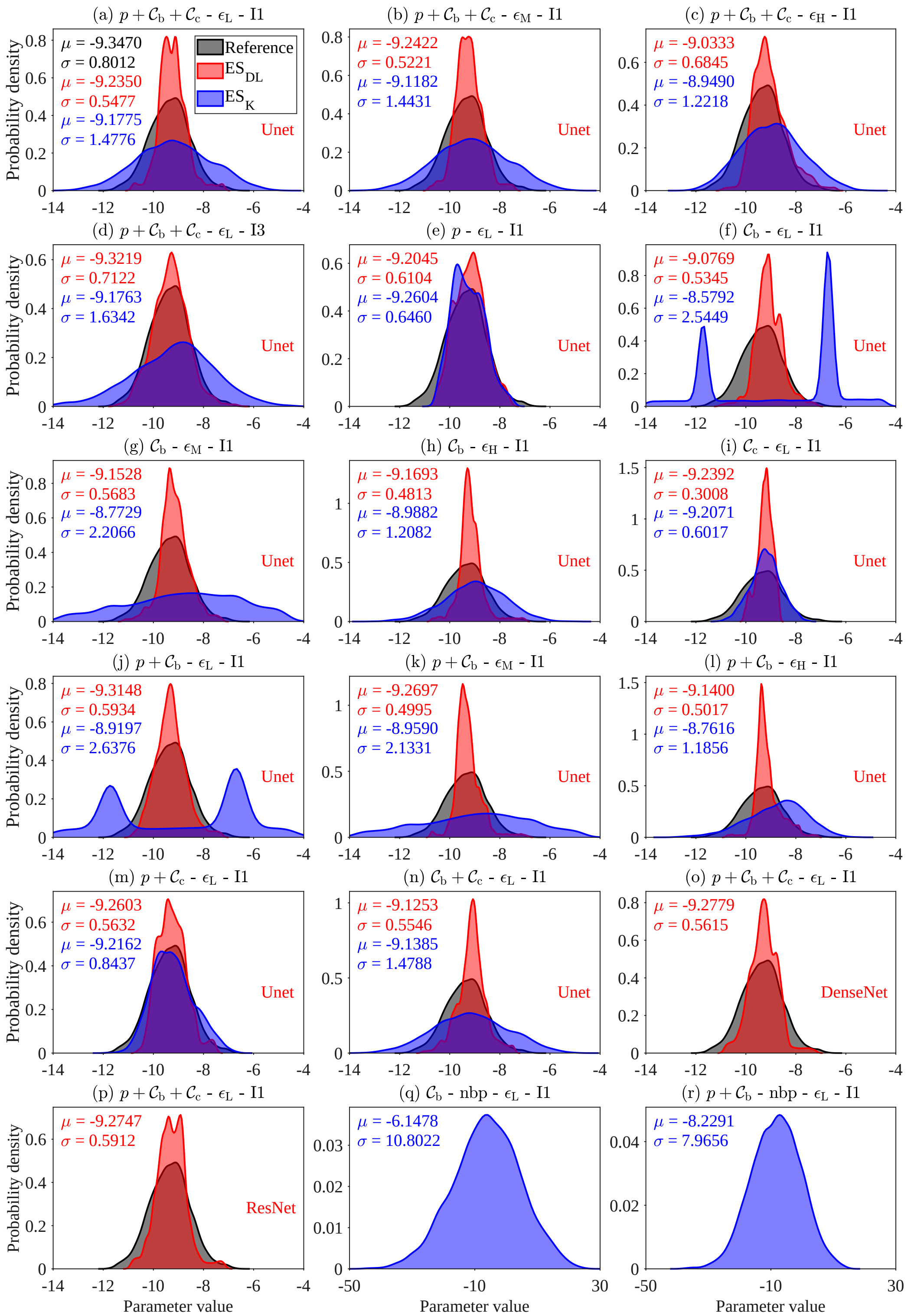

Figure 4. Probability density curves of the mean $\ln(\mathcal{K})$ fields obtained by $\mathrm{ES_{DL}}$ or $\mathrm{ES_K}$ with different settings in Case 1.

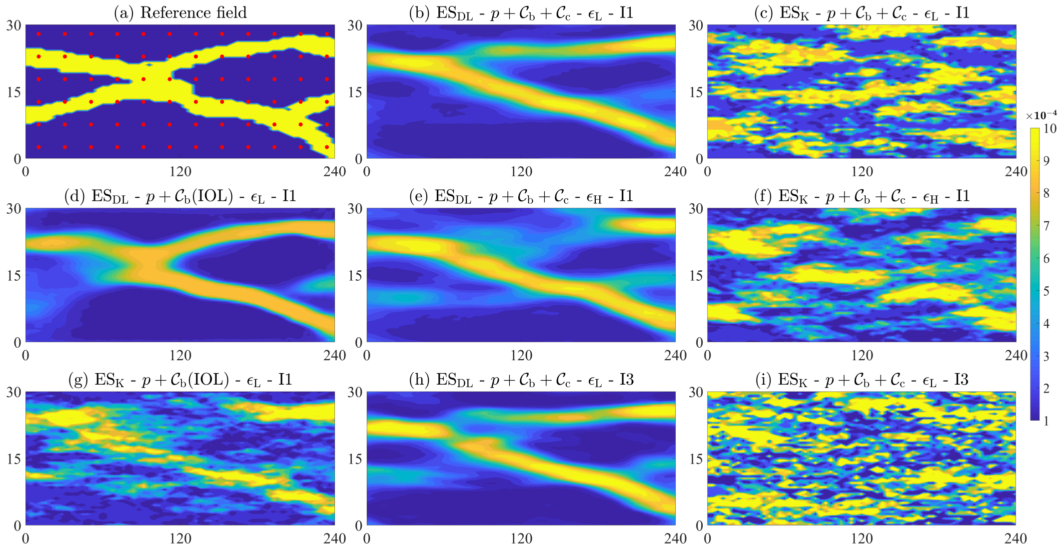

Figure 5. (a) The reference $\mathcal{K}$ field and distribution of the 6×12 observational locations in Case 2. (b-i) Mean fields of $\mathcal{K}$ obtained by $\mathrm{ES_{DL}}$ and $\mathrm{ES_K}$ with different settings indicated by the titles of the sub-figures. Here, $\mathrm{ES_{DL}}$ utilizes the Unet model, "IOL" indicates the condition with increased observational locations that has 15×48 wells uniformly distributed in the flow domain.

4.2 Case Study 2: Estimating Simple Binary Channelized Parameter Field

With a primary focus on assessing the effectiveness of $\mathrm{ES_{DL}}$ in characterizing non-Gaussian parameter fields, especially those exhibiting channelization patterns, we formulate two cases representing varying complexity levels. Case 2 revolves around a relatively simple channelized field, while Case 3 features a more intricate condition. Here, the parameter fields exhibit binary features (Figures 5a and 7a). In these scenarios, our investigation delves into strategies aimed at improving the characterization effectiveness of $\mathrm{ES_{DL}}$ under non-Gaussian conditions. This encompasses considerations such as optimal choices of data types, spatial distribution of measurement wells, and the iterative implementation of $\mathrm{ES_{DL}}$.

In the simpler case, we generate the reference (Figure 5a) and prior realizations of $\mathcal{K}$ field (61×61) with the direct sampling method proposed by Mariethoz et al. (2010). There are two distinct values of $\mathcal{K}$, i.e., $\mathcal{K}_1 = 10^{-4}$ m/s for the low permeable background, and $\mathcal{K}_2 = 10^{-3}$ m/s for the high permeable channels. In the numerical model, the interpolated $\mathcal{K}$ values are integrated into the model's triangulated grid network. We obtain observed values of p and C_b at moments of $t = 300, 600, ..., 1500, 2100, 2700, ..., 4500$ days, and C_c at $t = 1800, 2100, ..., 3000$ days, at the 6×12 locations marked by red dots in Figure 5(a). Consequently, the total number of observational data is $6\times12\times25$. It's noteworthy that the DL model used in this case study is Unet with the configuration of C2 in Table 2.

In this case study, we set the ensemble size as $N_\mathrm{e} = 500$ for both $\mathrm{ES_K}$ and $\mathrm{ES_{DL}}$. Figure 5(b) illustrates that when utilizing all measurement data at a low error magnitude (ϵ_L), $\mathrm{ES_{DL}}$ effectively captures channelized patterns in the reference field, achieving an average RMSE of 3.54×10^{-4}. Meanwhile, the average RMSE between the prior parameter ensemble and the reference $\mathcal{K}$ field is 5.65×10^{-4}. The update made by $\mathrm{ES_{DL}}$ signifies a notable reduction in parametric uncertainty. In contrast, $\mathrm{ES_K}$ yields significantly biased results (RMSE: 5.83×10^{-4}), as depicted in Figure 5(c). Upon increasing the error magnitude to ϵ_M, $\mathrm{ES_K}$ exhibits substantial improvement (RMSE: 4.41×10^{-4}), while $\mathrm{ES_{DL}}$ experiences slight degradation (RMSE: 3.70×10^{-4}), as observed in Figures 5(e-f). After three iterations (with ϵ_L), $\mathrm{ES_{DL}}$ demonstrates enhanced performance (RMSE: 2.99×10^{-4}), whereas

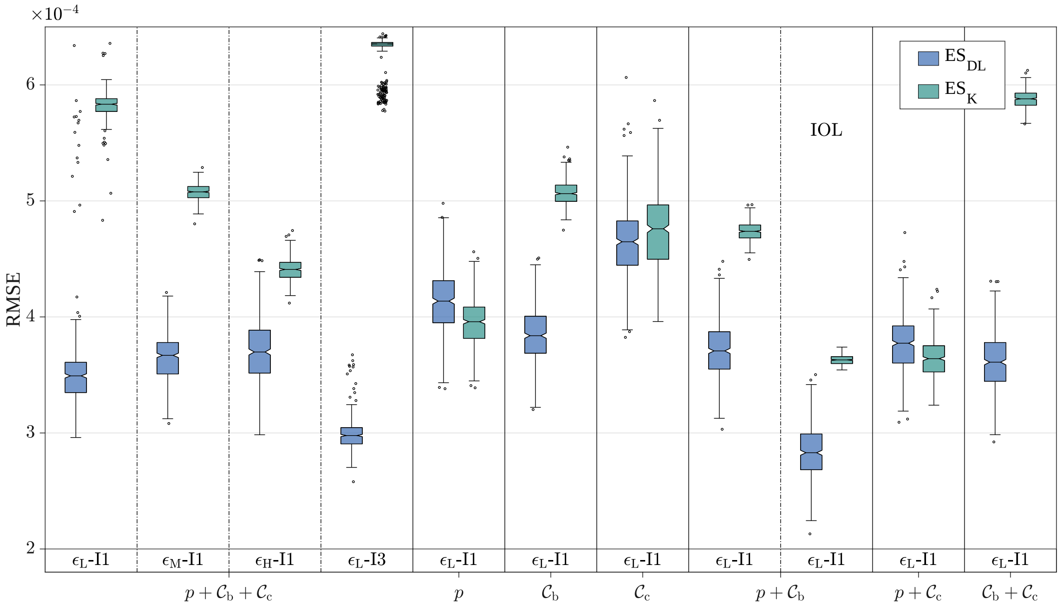

Figure 6. The RMSE values between the estimated $\mathcal{K}$ fields obtained by $\mathrm{ES_{DL}}/\mathrm{ES_{K}}$ and the reference field under different settings in Case 2. Here, "IOL" indicates the case with increased observational locations that has 15×48 measurement locations uniformed distributed in the flow domain. Here, $\mathrm{ES_{DL}}$ utilizes the Unet model.

$\mathrm{ES_K}$ shows the opposite trend (RMSE: 6.29×10^{-4}). For $\mathrm{ES_{DL}}$ to better capture the non-Gaussian features, acquiring additional measurement data to enhance information content regarding the unknown parameter field is advisable. To explore this further, we conduct a test with observations obtained from more locations and time steps (15×48 points uniformly distributed in the flow domain, with observation times the same as those in Case 1), denoted as "IOL" (increased observational locations). Figure 5(d) reveals that, with p and C_{b} data at the low measurement error magnitude, $\mathrm{ES_{DL}}$ (using the configuration of C6 in Table 2) achieves an improved characterization of the $\mathcal{K}$ field and a reduced average RMSE value of 2.83×10^{-4}. Switching to $\mathrm{ES_K}$ under these conditions also yields satisfactory results (RMSE: 3.63×10^{-4}), as depicted in Figure 5(g).

To comprehensively evaluate the performances of $\mathrm{ES_K}$ and $\mathrm{ES_{DL}}$ in characterizing the channelized $\mathcal{K}$ field, we plot RMSE values between the estimated and the reference $\mathcal{K}$ fields under various settings in Figure 6. The box-plots presented in this figure lead to the following findings. (1) The inversion results of $\mathrm{ES_K}$ exhibit significant variations across different types or combinations of observational data, with the optimal performance obtained when utilizing the "p+C_{c}" combination. In contrast, $\mathrm{ES_{DL}}$ demonstrates greater stability in estimation results across different data types or combinations. (2) For the $\mathrm{ES_K}$ method, an increase in observational error level ($\epsilon_{\mathrm{L}} \to \epsilon_{\mathrm{M}} \to \epsilon_{\mathrm{H}}$) reveals a decrease in the RMSE metrics when all three data types are used (see the first three columns of Figure 6). However, $\mathrm{ES_{DL}}$ exhibits a slight deterioration trend. (3) Implementing three iterations shows a noticeable decrease in RMSE for $\mathrm{ES_{DL}}$, while $\mathrm{ES_K}$ exhibits an increase, indicating the divergent outcome obtained by the Kalman update. (4) When the observational locations increase from 6×12 to 15×48, both $\mathrm{ES_K}$ and $\mathrm{ES_{DL}}$ will enjoy an improvement in performance, as shown in the eight and nine columns of Figure 6.

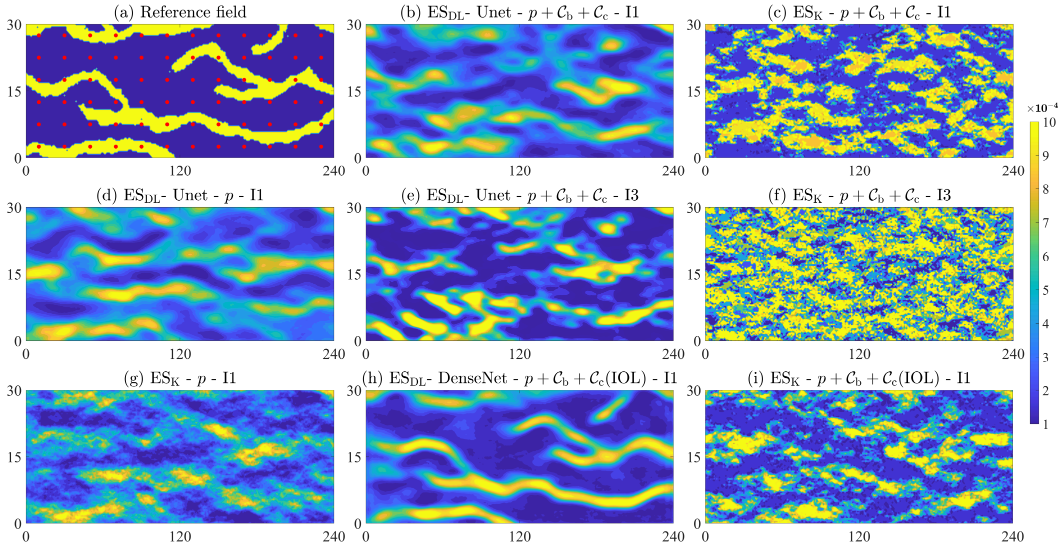

Figure 7. (a) The reference $\mathcal{K}$ field and distribution of 6×12 observational locations, (b-i) mean field of $\mathcal{K}$ estimated by $\mathrm{ES_{DL}}$ or $\mathrm{ES_K}$ with different settings in Case 3. Here, "IOL" indicates the condition with increased observational locations that has 12×24 wells uniformly distributed in the flow domain. In the above results, we only consider the low measurement error condition of ϵ_L.

4.3 Case Study 3: Estimating Complex Binary Channelized Parameter Field

In the previous section, we tested both $\mathrm{ES_K}$ and $\mathrm{ES_{DL}}$ in characterizing a relatively simple $\mathcal{K}$ field with channelized patterns. To assess their performances under more challenging conditions, we present a new case in this section. The reference field of $\mathcal{K}$ considered here is more complex, as illustrated in Figure 7(a). The dimension of this parameter field is 91×241, approximately six times larger than that in the previous case. In $\mathrm{ES_{DL}}$, we respectively utilize Unet, DenseNet, and ResNet with the C1, C7 (C8 for the "IOL" condition), and C7 configurations (Table 2) for comparison. In the "IOL" condition, 12×24 uniformly distributed measurement wells is considered. The other settings remain consistent with those of Case 2.

In Figure 7(b), utilizing the Unet-based $\mathrm{ES_{DL}}$ to assimilate "p+C_b+C_c" in a single iteration yields a mean field capturing only fragmented features of the reference field, struggling to properly represent the connectivity patterns provided by the channels. Nevertheless, the resulting average RMSE (4.26×10^{-4}) is significantly lower than the average RMSE (5.65×10^{-4}) of the prior ensemble. Likewise, increasing the iteration number (Figure 7e, RMSE: 3.88×10^{-4}) and observational wells (Figure 7h, RMSE: 3.32×10^{-4}) can enhance the performance of $\mathrm{ES_{DL}}$. For $\mathrm{ES_K}$, however, increasing the observational wells improves the performance, while increasing the iteration number diminishes the effectiveness of the Kalman update, as depicted in Figures 7(c), (f), and (i), with respective RMSEs of 5.75×10^{-4}, 6.47×10^{-4}, and 4.52×10^{-4}. When exclusively using p data obtained from a more linear and continuous hydraulic process, $\mathrm{ES_K}$ achieves reasonable results (Figure 7g, RMSE: 4.54×10^{-4}), albeit superior to $\mathrm{ES_{DL}}$ (Figure 7d, RMSE: 5.07×10^{-4}). Overall, this case presents greater challenges, yet still underscores the robustness of $\mathrm{ES_{DL}}$.

In Figure 8, we conduct a comprehensive comparison of the RMSE values obtained through $\mathrm{ES_K}$/$\mathrm{ES_{DL}}$ under various settings. The primary findings are outlined as follows. Generally, $\mathrm{ES_{DL}}$ demonstrates more robust results compared to $\mathrm{ES_K}$. For this complex case, using all three data types can produce the best performance for $\mathrm{ES_{DL}}$. Notably, in the

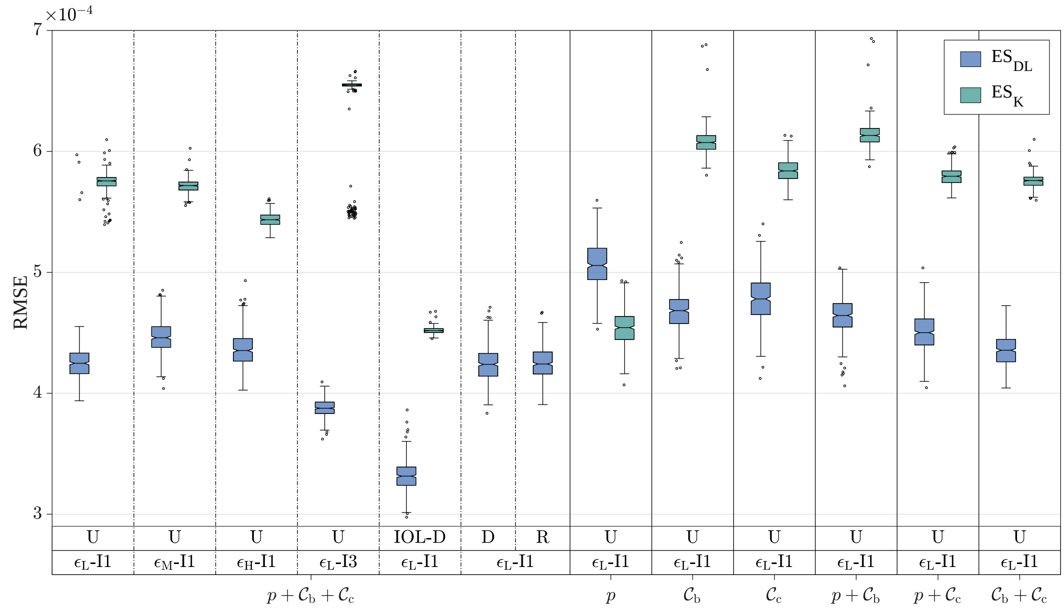

Figure 8. The RMSE values between the estimated $\mathcal{K}$ fields obtained by $\mathrm{ES_{DL}}/\mathrm{ES_K}$ and the reference field in Case 3. Here, "IOL" indicates the case with increased observational locations that has 12×24 points uniformed distributed in the flow domain. "U", "D", and "R" denote the Unet, DenseNet, and ResNet models used in $\mathrm{ES_{DL}}$, respectively.

case of the "p-ϵ_{L}-I1" setting, it is interesting to observe that $\mathrm{ES_K}$ outperforms Unet-based $\mathrm{ES_{DL}}$. This phenomenon may arise from the inherent complexity of the problem and the sub-optimal configuration of the Unet model and training options. The three DL models yield comparable results in $\mathrm{ES_{DL}}$, and considering the shortest training time needed for training Unet, this DL model is recommended for practical use.

4.4 Case Study 4: Estimating Continuous Channelized Parameter Field

In practical applications, variations exist in both the high and low permeable regions of the $\mathcal{K}$ field. In our final case study, we consider a more realistic scenario involving a continuous channelized $\mathcal{K}$ field. Illustrated in Figure 9(a), a 91×241 dimensional reference $\mathcal{K}$ field is generated by adding a binary field ($\mathcal{K}_1 = 1 \times 10^{-4}$, $\mathcal{K}_2 = 5 \times 10^{-4}$) with a Gaussian distributed field ($\mu = 0$, $\sigma = 0.2$). This reference field exhibits a Gaussian mixture distribution, as shown in Figure 11 (the blue curves). In this case study, the Unet, DenseNet, and ResNet models used in $\mathrm{ES_{DL}}$ correspond to the training configurations of C3, C9, and C7 in Table 2. The other settings remain consistent with those of Case 3.

In Figures 9(b-i), we illustrate the estimated mean fields of $\mathcal{K}$ using $\mathrm{ES_K}/\mathrm{ES_{DL}}$ across various settings. The corresponding average RMSE values are 1.98×10^{-4}, 3.42×10^{-4}, 1.93×10^{-4}, 2.38×10^{-4}, 2.06×10^{-4}, 1.93×10^{-4}, 1.61×10^{-4}, and 2.12×10^{-4}, respectively. For reference, the average RMSE value of the prior parameter ensemble is 2.52×10^{-4}. Notably, it is pleasing to observe that $\mathrm{ES_{DL}}$ using ResNet achieves a robust characterization of the $\mathcal{K}$ field without the need for additional measurement locations, as exemplified in Figure 9(g). It indicates that in this complex problem, the choice of the DL model plays a vital role in the performance of $\mathrm{ES_{DL}}$. Other findings are similar to the previous cases.

In Figure 10, we conduct a comprehensive comparison of RMSEs obtained through $\mathrm{ES_{DL}}$ and $\mathrm{ES_K}$ across a broader range of settings. In this intricate scenario, we note the

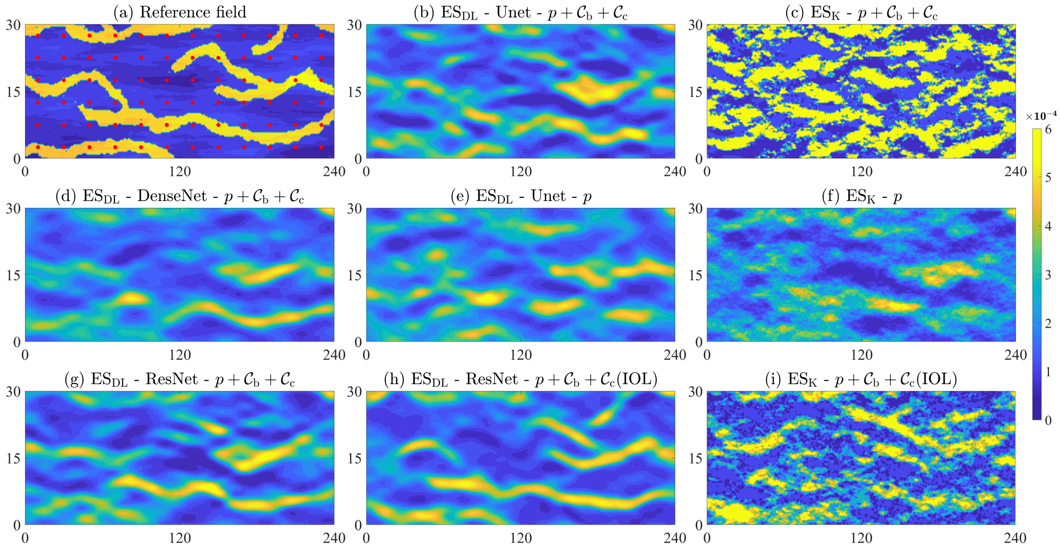

Figure 9. (a) The reference $\mathcal{K}$ field and distribution of 6×12 observational locations, (b-i) mean fields of $\mathcal{K}$ estimated by ES$_{\mathrm{DL}}$/ES$_{\mathrm{K}}$ with different settings in Case 4. Here, "IOL" indicates the condition with increased observational locations that has 12×24 wells uniformly distributed in the flow domain. In the above results, we only consider the low measurement error condition of ϵ_{L} and perform one iteration.

consistent robustness of ES$_{\mathrm{DL}}$ across diverse configurations. However, it is interesting to observe instances where ES$_{\mathrm{K}}$ outperforms ES$_{\mathrm{DL}}$, particularly in cases such as when only p or C_{c} data aer utilized with ϵ_{L} in a single iteration (the 8th and 10th columns of Figure 10). This discrepancy may be attributed to the heightened continuity of the $\mathcal{K}$ field in comparison to Cases 2-3. In the context of ES$_{\mathrm{K}}$, it exhibits results with decreased performance whenever C_{b} is employed, except in scenarios with increased observational locations. Notably, for ES$_{\mathrm{DL}}$, employing three iterations may yield less accurate parameter field estimates compared to a single iteration, as evidenced by the comparison between the first and fourth columns of Figure 10.

Moreover, we present the probability density curves depicting the reference and estimated $\mathcal{K}$ fields by ES$_{\mathrm{DL}}$ and ES$_{\mathrm{K}}$ under various algorithmic settings. Notably, ES$_{\mathrm{DL}}$ demonstrates a higher frequency of instances where the bi-modal distribution of $\mathcal{K}$ can be identified to a certain extent. It is essential to highlight that a more accurate identification of the bi-modality in $\mathcal{K}$ does not correspond to a more precise estimation of the parameter field, reflected in a smaller RMSE value. For instance, in Figure 11(h), ES$_{\mathrm{DL}}$ achieves the optimal match of bi-modality, despite the related RMSE value being marginally larger than that of ES$_{\mathrm{K}}$ using the same settings. However, Figure 11 serves as a comprehensive indicator of the overall effectiveness of a DA method in characterizing non-Gaussian parameter fields. On the other hand, for ES$_{\mathrm{K}}$, the identification of the bi-modal distribution of $\mathcal{K}$ is either unsuccessful (e.g., Figure 11f) or inaccurate (e.g., Figure 11e). Notably, the peak values of the density curves obtained by ES$_{\mathrm{K}}$ consistently deviate from the reference values, underscoring the method's vulnerability in addressing non-Gaussian DA problems.

Despite the considerable capability of ES$_{\mathrm{DL}}$ in addressing non-linear and non-Gaussian DA problems, achieving a robust alignment with the reference distribution curve of $\mathcal{K}$ in this particular scenario still poses a persistent challenge. To enhance the performance of ES$_{\mathrm{DL}}$, several strategic approaches can be implemented. Firstly, one effective tactic involves increasing the ensemble size N_{e}. By doing so, a larger volume of training data can be

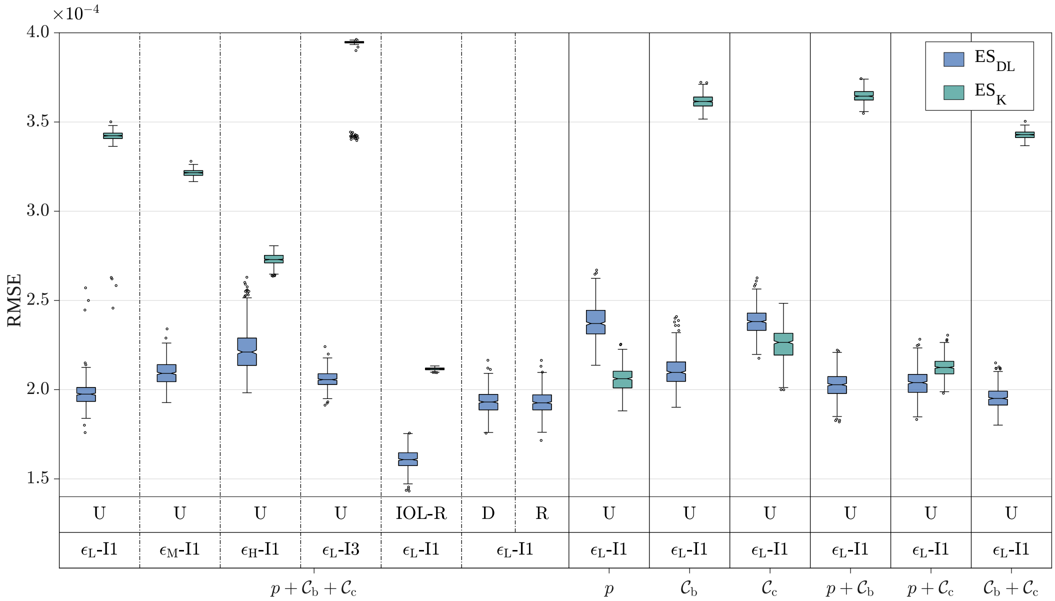

Figure 10. Comparison of RMSEs values between the estimated $\mathcal{K}$ fields obtained by $\mathrm{ES_{DL}}/\mathrm{ES_K}$ and the reference field in Case 4. Here, "IOL" indicates the case with increased observational locations that has 12×24 points uniformed distributed in the flow domain. "U", "D", and "R" denote the Unet, DenseNet, and ResNet models, respectively. Additionally, "I1" and "I3" represent one iteration and three iterations, respectively.

acquired, thereby enhancing the generalization capabilities of the DL model. Secondly, there is a crucial need to refine the architectures of the DL model and optimize training configurations. While this study employed three widely used DL models (i.e., Unet, ResNet, and DenseNet), acknowledging the potential for more suitable design in model architectures is essential for continued improvement. Thirdly, to augment the information content of the measurement data and concurrently reduce sampling costs, it is recommended to undertake optimal experiment design. This involves strategic decisions on where, when, and what types of data to collect, ensuring a more efficient and informative data acquisition process for our task at hand.

5 Conclusions

SI poses a significant threat to coastal groundwater systems. effectively preventing and controlling SI involve conducting predictive analyses and scenario studies based on numerical models. A crucial prerequisite for achieving this goal is the precise characterization of heterogeneity in coastal aquifers through DA. Traditional DA methods face challenges in obtaining reliable results when dealing with non-linear processes and non-Gaussian parameters/states.

In this study, we advocate for employing a DL-based DA method, specifically $\mathrm{ES_{DL}}$, to robustly characterize heterogeneous coastal aquifers. To demonstrate the method's efficacy and constraints, we systematically explore various factors influencing its performance, including the number and types of observations, the degree of aquifer heterogeneity, and the structural and training options of the DL model. Four case studies, incrementally increasing in complexity, are devised, and we implement the classical DA method based on the Kalman update, denoted as $\mathrm{ES_K}$, for comparative analysis. Through methodical experimentation, the study reveals the following key findings.

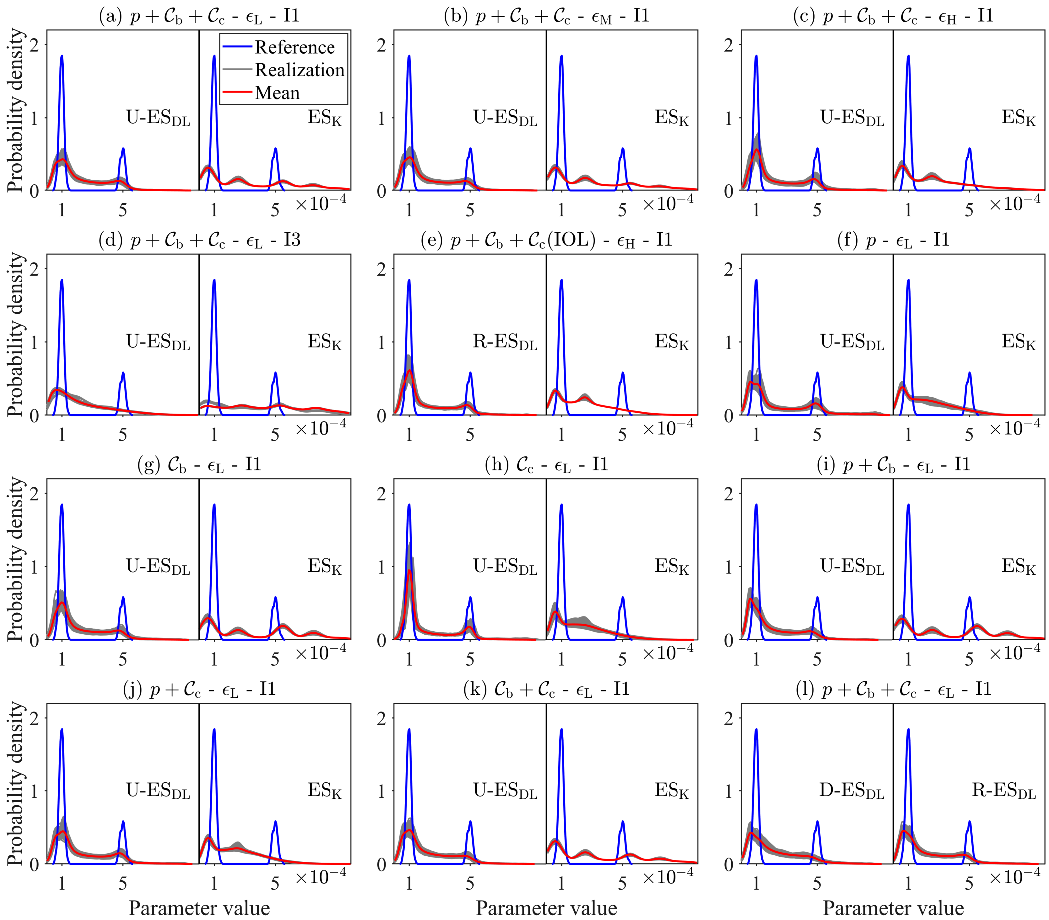

Figure 11. Probability density curves of the estimated $\mathcal{K}$ fields obtained by ES$_{DL}$ and ES$_K$ with different settings in Case 4.

(1) $\mathrm{ES_K}$ consistently falls short in providing satisfactory characterization of hydraulic conductivity fields, whether in Gaussian or various non-Gaussian forms. Even in scenarios where $\mathrm{ES_K}$ is expected to excel, such as Gaussian cases, divergent updating outcomes emerge when highly non-linear processes are involved, e.g., when utilizing C_b data. $\mathrm{ES_K}$ performs adequately only when assimilating p data from relatively linear and continuous processes. Interestingly, when incorporating all three data types (p, C_b, and C_c), increasing the iteration number exacerbates the deterioration of $\mathrm{ES_K}$ outcomes. However, elevating the magnitude of measurement error provides a modest mitigation of updating divergence, leading to a slight improvement in estimation accuracy, which is different from $\mathrm{ES_{DL}}$.

(2) $\mathrm{ES_{DL}}$ consistently demonstrates robust performance across all case studies with varying settings, particularly when paired with a suitable DL model such as Unet, DenseNet, or ResNet. Enhancing the iteration number or increasing the volume of measurement data consistently contributes to the improved performance of this DA method. Notably, when the target parameter field displays bi-modal distribution characteristics, $\mathrm{ES_{DL}}$ exhibits the capability to partially replicate this feature in its estimation results. In a few tests of Case 4, the performance of $\mathrm{ES_{DL}}$ is still not good enough. To optimize the efficacy of $\mathrm{ES_{DL}}$, meticulous attention must be given to the design of the DL model and the selection of training options. Furthermore, to provide more informative data for DA, it is recommended to implement optimal design strategies for selecting locations, times, and types of data, considering constraints such as budget limitations.

Open Research

The data and codes on which this article is based are available in (C. Cao & Zhang, 2023).

Acknowledgments

This study is supported by the National Key R&D Program of China (grant 2021YFC3200500), Jiangsu Provincial Innovation and Entrepreneurship Doctor Program (grant JSSCBS20210260), Natural Science Foundation of Jiangsu Province (grant BK20231461), and National Natural Science Foundation of China (grants 52121006 and 42007004).

References

Beaujean, J., Nguyen, F., Kemna, A., Antonsson, A., & Engesgaard, P. (2014). Calibration of seawater intrusion models: Inverse parameter estimation using surface electrical resistivity tomography and borehole data. *Water Resources Research*, *50*(8), 6828–6849. doi: 10.1002/2013WR014020

Blanco-Coronas, A., Duque, C., Calvache, M., & López-Chicano, M. (2021). Temperature distribution in coastal aquifers: Insights from groundwater modeling and field data. *Journal of Hydrology*, *603*, 126912. doi: 10.1016/j.jhydrol.2021.126912

Brunetti, C., & Linde, N. (2018). Impact of petrophysical uncertainty on bayesian hydrogeophysical inversion and model selection. *Advances in Water Resources*, *111*, 346–359. doi: 10.1016/j.advwatres.2017.11.028

Canchumuni, S. A., Emerick, A. A., & Pacheco, M. A. (2017). Integration of ensemble data assimilation and deep learning for history matching facies models. In *Offshore Technology Conference Brasil* (p. D011S006R005). doi: 10.4043/28015-MS

Cao, C., & Zhang, J. (2023). *MATLAB Codes for the Paper "Characterization of Heterogeneous Coastal Aquifers Using A Deep Learning-Based Data Assimilation Approach" [Software]*. figshare. https://doi.org/10.6084/m9.figshare.24773757.

Cao, T., Han, D., & Song, X. (2021). Past, present, and future of global seawater intrusion research: A bibliometric analysis. *Journal of Hydrology*, *603*, 126844. doi: 10.1016/j.jhydrol.2021.126844

Chang, H., Zhang, D., & Lu, Z. (2010). History matching of facies distribution with the EnKF and level set parameterization. *Journal of Computational Physics*, *229*(20), 8011–8030. doi: 10.1016/j.jcp.2010.07.005

Coulon, C., Pryet, A., Lemieux, J.-M., Yrro, B. J. F., Bouchedda, A., Gloaguen, E., ... Banton, O. (2021). A framework for parameter estimation using sharp-interface seawater intrusion models. *Journal of Hydrology*, *600*, 126509. doi: 10.1016/j.jhydrol.2021.126509

Custodio, E. (2010). Coastal aquifers of Europe: an overview. *Hydrogeology Journal*, *18*(1), 269. doi: 10.1007/s10040-009-0496-1

Deutsch, & Journel. (1998). *GSLIB: Geostatistical software library and users guide*. Oxford University Press.

Dodangeh, A., Rajabi, M. M., Carrera, J., & Fahs, M. (2022). Joint identification of contaminant source characteristics and hydraulic conductivity in a tide-influenced coastal aquifer. *Journal of Contaminant Hydrology*, *247*, 103980. doi: 10.1016/j.jconhyd.2022.103980

Elsheikh, A. H., Wheeler, M. F., & Hoteit, I. (2013). Clustered iterative stochastic ensemble method for multi-modal calibration of subsurface flow models. *Journal of Hydrology*, *491*, 40–55. doi: 10.1016/j.jhydrol.2013.03.037

Evensen, G. (1994). Sequential data assimilation with a nonlinear quasi-geostrophic model using Monte Carlo methods to forecast error statistics. *Journal of Geophysical Research: Oceans*, *99*(C5), 10143–10162. doi: 10.1029/94JC00572

Folch, A., del Val, L., Luquot, L., Martínez-Pérez, L., Bellmunt, F., Le Lay, H., ... Carrera, J. (2020). Combining fiber optic DTS, cross-hole ERT and time-lapse induction logging to characterize and monitor a coastal aquifer. *Journal of Hydrology*, *588*, 125050. doi: 10.1016/j.jhydrol.2020.125050

Freeze, R. A. (1975). A stochastic-conceptual analysis of one-dimensional groundwater flow in nonuniform homogeneous media. *Water Resources Research*, *11*(5), 725–741. doi: 10.1029/WR011i005p00725

Geng, X., & Michael, H. A. (2020). Preferential flow enhances pumping-induced saltwater intrusion in volcanic aquifers. *Water Resources Research*, *56*(5), e2019WR026390. doi: 10.1029/2019WR026390

Godoy, V. A., Napa-García, G. F., & Gómez-Hernández, J. J. (2022). Ensemble random forest filter: An alternative to the ensemble kalman filter for inverse modeling. *Journal of Hydrology*, *615*, 128642. doi: 10.1016/j.jhydrol.2022.128642

Goebel, M., Pidlisecky, A., & Knight, R. (2017). Resistivity imaging reveals complex pattern of saltwater intrusion along Monterey coast. *Journal of Hydrology*, *551*, 746–755. doi: 10.1016/j.jhydrol.2017.02.037

González-Quirós, A., & Comte, J.-C. (2020). Relative importance of conceptual and computational errors when delineating saltwater intrusion from resistivity inverse models in heterogeneous coastal aquifers. *Advances in Water Resources*, *144*, 103695. doi: 10.1016/j.advwatres.2020.103695

Han, D., & Currell, M. J. (2018). Delineating multiple salinization processes in a coastal plain aquifer, northern China: hydrochemical and isotopic evidence. *Hydrology and Earth System Sciences*, *22*(6), 3473–3491. doi: 10.5194/hess-22-3473-2018

Han, Z., Kang, X., Wu, J., & Shi, X. (2022). Characterization of the non-Gaussian hydraulic conductivity field via deep learning-based inversion of hydraulic-head and self-potential data. *Journal of Hydrology*, *610*, 127830. doi: 10.1016/j.jhydrol.2022.127830

He, K., Zhang, X., Ren, S., & Sun, J. (2016). Deep residual learning for image recognition. In *Proceedings of the IEEE Conference on Computer Vision and Pattern Recognition* (pp. 770–778). doi: 10.1109/CVPR.2016.90

Huang, G., Liu, Z., Van Der Maaten, L., & Weinberger, K. Q. (2017). Densely connected convolutional networks. In *Proceedings of the IEEE Conference on Computer Vision and Pattern Recognition* (pp. 4700–4708). doi: 10.1109/CVPR.2016.90

Jung, H., Jo, H., Kim, S., Lee, K., & Choe, J. (2017). Recursive update of channel information for reliable history matching of channel reservoirs using EnKF with DCT.

Journal of Petroleum Science and Engineering, *154*, 19–37. doi: 10.1016/j.petrol.2017.04.016
Kang, P. K., Lee, J., Fu, X., Lee, S., Kitanidis, P. K., & Juanes, R. (2017). Improved characterization of heterogeneous permeability in saline aquifers from transient pressure data during freshwater injection. *Water Resources Research*, *53*(5), 4444–4458. doi: 10.1002/2016WR020089
Kang, X., Shi, X., Revil, A., Cao, Z., Li, L., Lan, T., & Wu, J. (2019). Coupled hydrogeophysical inversion to identify non-Gaussian hydraulic conductivity field by jointly assimilating geochemical and time-lapse geophysical data. *Journal of Hydrology*, *578*, 124092. doi: 10.1016/j.jhydrol.2019.124092
Koohbor, B., Fahs, M., Ataie-Ashtiani, B., Belfort, B., Simmons, C. T., & Younes, A. (2019). Uncertainty analysis for seawater intrusion in fractured coastal aquifers: Effects of fracture location, aperture, density and hydrodynamic parameters. *Journal of Hydrology*, *571*, 159–177. doi: 10.1016/j.jhydrol.2019.01.052
Li, L., Stetler, L., Cao, Z., & Davis, A. (2018). An iterative normal-score ensemble smoother for dealing with non-Gaussianity in data assimilation. *Journal of Hydrology*, *567*, 759–766. doi: 10.1016/j.jhydrol.2018.01.038
Lu, C., Chen, Y., Zhang, C., & Luo, J. (2013). Steady-state freshwater–seawater mixing zone in stratified coastal aquifers. *Journal of Hydrology*, *505*, 24–34. doi: 10.1016/j.jhydrol.2013.09.017
Lu, C., Werner, A. D., Simmons, C. T., Robinson, N. I., & Luo, J. (2013). Maximizing net extraction using an injection-extraction well pair in a coastal aquifer. *Groundwater*, *51*(2), 219–228. doi: 10.1111/j.1745-6584.2012.00973.x
Man, J., Guo, Y., Jin, J., Zhang, J., Yao, Y., & Zhang, J. (2022). Characterization of vapor intrusion sites with a deep learning-based data assimilation method. *Journal of Hazardous Materials*, *431*, 128600. doi: 10.1016/j.jhazmat.2022.128600
Mantoglou, A. (2003). Pumping management of coastal aquifers using analytical models of saltwater intrusion. *Water Resources Research*, *39*(12), 1335. doi: 10.1029/2002WR001891
Mariethoz, G., Renard, P., & Straubhaar, J. (2010). The direct sampling method to perform multiple-point geostatistical simulations. *Water Resources Research*, *46*(11), W11536. doi: 10.1029/2008WR007621
McCurry, J., Poterjoy, J., Knopfmeier, K., & Wicker, L. (2023). An evaluation of non-gaussian data assimilation methods in moist convective regimes. *Monthly Weather Review*, *151*(7), 1609–1629. doi: 10.1175/MWR-D-22-0260.1
Michael, H. A., Mulligan, A. E., & Harvey, C. F. (2005). Seasonal oscillations in water exchange between aquifers and the coastal ocean. *Nature*, *436*(7054), 1145–1148. doi: 10.1038/nature0393
Paldor, A., & Michael, H. (2021). Storm surges cause simultaneous salinization and freshening of coastal aquifers, exacerbated by climate change. *Water Resources Research*, *57*(5), e2020WR029213. doi: 10.1029/2020WR029213
Park, N., Cui, L., & Shi, L. (2009). Analytical design curves to maximize pumping or minimize injection in coastal aquifers. *Groundwater*, *47*(6), 797–805. doi: 10.1111/j.1745-6584.2009.00589.x
Renard, P., & Allard, D. (2013). Connectivity metrics for subsurface flow and transport. *Advances in Water Resources*, *51*, 168–196. doi: 10.1016/j.advwatres.2011.12.001
Riva, M., Guadagnini, A., & Dell'Oca, A. (2015). Probabilistic assessment of seawater intrusion under multiple sources of uncertainty. *Advances in Water Resources*, *75*, 93–104. doi: 10.1016/j.advwatres.2014.11.002
Ronneberger, O., Fischer, P., & Brox, T. (2015). U-Net: convolutional networks for biomedical image segmentation. In *Medical Image Computing and Computer-Assisted Intervention – MICCAI 2015* (pp. 234–241). Springer International Publishing.
Schöniger, A., Nowak, W., & Hendricks Franssen, H.-J. (2012). Parameter estimation by ensemble Kalman filters with transformed data: Approach and application to hydraulic tomography. *Water Resources Research*, *48*(4). doi: 10.1029/2011WR010462

Sciortino, A., Harmon, T. C., & Yeh, W. W.-G. (2002). Experimental design and model parameter estimation for locating a dissolving dense nonaqueous phase liquid pool in groundwater. *Water Resources Research*, *38*(5), 15–1. doi: 10.1029/2000WR000134

Sendrós, A., Urruela, A., Himi, M., Alonso, C., Lovera, R., Tapias, J. C., ... Casas, A. (2021). Characterization of a shallow coastal aquifer in the framework of a subsurface storage and soil aquifer treatment project using electrical resistivity tomography (port de la selva, spain). *Applied Sciences*, *11*(6), 2448. doi: 10.3390/app11062448

Sherlock, M. D., Chappell, N. A., & McDonnell, J. J. (2000). Effects of experimental uncertainty on the calculation of hillslope flow paths. *Hydrological Processes*, *14*(14), 2457–2471. doi: 10.1002/1099-1085(20001015)14:14⟨2457::AID-HYP106⟩3.0.CO;2-I

Shi, L., Lu, C., Ye, Y., Xie, Y., & Wu, J. (2020). Evaluation of the performance of multiple-well hydraulic barriers on enhancing groundwater extraction in a coastal aquifer. *Advances in Water Resources*, *144*, 103704. doi: 10.1016/j.advwatres.2020.103704

Sihag, P., Mohsenzadeh Karimi, S., & Angelaki, A. (2019). Random forest, M5P and regression analysis to estimate the field unsaturated hydraulic conductivity. *Applied Water Science*, *9*, 1–9. doi: 10.1007/s13201-019-1007-8

Song, J., Yang, Y., Wu, J., Wu, J., Sun, X., & Lin, J. (2018). Adaptive surrogate model based multiobjective optimization for coastal aquifer management. *Journal of Hydrology*, *561*, 98–111. doi: 10.1016/j.jhydrol.2018.03.063

Strack, O. (1976). A single-potential solution for regional interface problems in coastal aquifers. *Water Resources Research*, *12*(6), 1165–1174. doi: 10.1029/WR012i006p01165

Trabucchi, M., Fernàndez-Garcia, D., & Carrera, J. (2022). The worth of stochastic inversion for identifying connectivity by means of a long-lasting large-scale hydraulic test: The salar de atacama case study. *Water Resources Research*, *58*(6), e2021WR030676. doi: 10.1029/2021WR030676

Van Leeuwen, P. J., & Evensen, G. (1996). Data assimilation and inverse methods in terms of a probabilistic formulation. *Monthly Weather Review*, *124*(12), 2898–2913. doi: 10.1175/1520-0493(1996)124⟨2898:DAAIMI⟩2.0.CO;2

Vo, H. X., & Durlofsky, L. J. (2014). A new differentiable parameterization based on principal component analysis for the low-dimensional representation of complex geological models. *Mathematical Geosciences*, *46*, 775–813. doi: 10.1007/s11004-014-9541-2

Voss, C. I., & Provost, A. M. (2002). *SUTRA: A model for 2D or 3D saturated-unsaturated, variable-density ground-water flow with solute or energy transport* (Tech. Rep.). US Geological Survey. doi: 10.3133/wri024231

Wang, Y., & Yan, B. (2022). On the feasibility of an ensemble multi-fidelity neural network for fast data assimilation for subsurface flow in porous media. *Available at SSRN 4293917*. doi: 10.2139/ssrn.4293917

Werner, A. D. (2010). A review of seawater intrusion and its management in Australia. *Hydrogeology Journal*, *1*(18), 281–285. doi: 10.1007/s10040-009-0465-8

Werner, A. D., Bakker, M., Post, V. E., Vandenbohede, A., Lu, C., Ataie-Ashtiani, B., ... Barry, D. A. (2013). Seawater intrusion processes, investigation and management: recent advances and future challenges. *Advances in Water Resources*, *51*, 3–26. doi: 10.1016/j.advwatres.2012.03.004

Xiao, C., Zhang, S., Ma, X., Zhou, T., Hou, T., & Chen, F. (2023). Deep-learning-generalized data-space inversion and uncertainty quantification framework for accelerating geological CO_2 plume migration monitoring. *Geoenergy Science and Engineering*, *224*, 211627. doi: 10.1016/j.geoen.2023.211627

Xu, Z., Hariharan, J., Passalacqua, P., Steel, E., Chadwick, A., Paola, C., ... Michael, H. A. (2022). Effects of geologic setting on contaminant transport in deltaic aquifers. *Water Resources Research*, *58*(9), e2022WR031943. doi: 10.1029/2022WR031943

Yang, H., Sun, H., Liu, T., Yang, X., Yang, F., & Jiao, J. (2023). Characterization of seawater intrusion based on machine learning and implications for offshore management under shared socioeconomic paths. *Journal of Hydrology*, *623*, 129862. doi: 10.1016/j.jhydrol.2023.129862

Yin, J., Tsai, F. T.-C., & Lu, C. (2022). Bi-objective extraction-injection optimization modeling for saltwater intrusion control considering surrogate model uncertainty. *Water Resources Management*, *36*(15), 6017–6042. doi: 10.1007/s11269-022-03340-9

Yoon, S., Lee, S., Williams, J. R., & Kang, P. K. (2020). Effects of variable-density flow on the value-of-information of pressure and concentration data for aquifer characterization. *Advances in Water Resources*, *135*, 103468. doi: 10.1016/j.advwatres.2019.103468

Yoon, S., Williams, J. R., Juanes, R., & Kang, P. K. (2017). Maximizing the value of pressure data in saline aquifer characterization. *Advances in Water Resources*, *109*, 14–28. doi: 10.1016/j.advwatres.2017.08.019

Yu, X., & Michael, H. A. (2019). Mechanisms, configuration typology, and vulnerability of pumping-induced seawater intrusion in heterogeneous aquifers. *Advances in Water Resources*, *128*, 117–128. doi: 10.1016/j.advwatres.2019.04.013

Yu, X., & Michael, H. A. (2022). Impacts of the scale of representation of heterogeneity on simulated salinity and saltwater circulation in coastal aquifers. *Water Resources Research*, *58*(1), e2020WR029523. doi: 10.1029/2020WR029523

Zhang, J., Cao, C., Nan, T., Ju, L., Zhou, H., & Zeng, L. (2023). A novel deep learning approach for data assimilation of complex hydrological systems. *Authorea Preprints*. doi: 10.22541/essoar.168565409.90872406/v1

Zhang, J., Lin, G., Li, W., Wu, L., & Zeng, L. (2018). An iterative local updating ensemble smoother for estimation and uncertainty assessment of hydrologic model parameters with multimodal distributions. *Water Resources Research*, *54*(3), 1716–1733. doi: 10.1002/2017WR020906

Zhang, J., Vrugt, J. A., Shi, X., Lin, G., Wu, L., & Zeng, L. (2020). Improving simulation efficiency of mcmc for inverse modeling of hydrologic systems with a kalman-inspired proposal distribution. *Water Resources Research*, *56*(3), e2019WR025474. doi: 10.1029/2019WR025474

Zhang, J., Zeng, L., Chen, C., Chen, D., & Wu, L. (2015). Efficient Bayesian experimental design for contaminant source identification. *Water Resources Research*, *51*(1), 576–598. doi: 10.1002/2014WR015740

Zhang, J., Zheng, Q., Wu, L., & Zeng, L. (2020). Using deep learning to improve ensemble smoother: Applications to subsurface characterization. *Water Resources Research*, *56*(12), e2020WR027399. doi: 10.1029/2020WR027399

Zhou, H., Gomez-Hernandez, J. J., Franssen, H.-J. H., & Li, L. (2011). An approach to handling non-Gaussianity of parameters and state variables in ensemble Kalman filtering. *Advances in Water Resources*, *34*(7), 844–864. doi: 10.1016/j.advwatres.2011.04.014

Zhou, H., Gómez-Hernández, J. J., & Li, L. (2014). Inverse methods in hydrogeology: Evolution and recent trends. *Advances in Water Resources*, *63*, 22–37. doi: 10.1016/j.advwatres.2013.10.014

Zinn, B., & Harvey, C. F. (2003). When good statistical models of aquifer heterogeneity go bad: A comparison of flow, dispersion, and mass transfer in connected and multivariate Gaussian hydraulic conductivity fields. *Water Resources Research*, *39*(3), 1051. doi: 10.1029/2001WR001146